Giant magnetocaloric effect in magnets down to the monolayer limit

Weiwei He Yan Yin Qihua Gong Richard F. L. Evans Oliver Gutfleisch Baixiang Xu Min Yi* Wanlin Guo**

W. He, Y. Yin, Q. Gong, M. Yi, W. Guo
State Key Lab of Mechanics and Control of Mechanical Structures & Key Lab for Intelligent Nano Materials and Devices of Ministry of Education & Institute for Frontier Science, Nanjing University of Aeronautics and Astronautics (NUAA), Nanjing 210016, China
Email Address: gongqihua@nuaa.edu.cn; yimin@nuaa.edu.cn; wlguo@nuaa.edu.cn
R. F. L. Evans
Department of Physics, The University of York, York YO105DD, United Kingdom
O. Gutfleisch, B. Xu
Institute of Materials Science, Technische Universität Darmstadt, Darmstadt 64287, Germany

Keywords: *2D magnets, isothermal magnetic entropy change, adiabatic temperature change, specific cooling power, strain tunability*

arXiv:2303.15722v1 [cond-mat.mtrl-sci] 28 Mar 2023

Two-dimensional magnets could potentially revolutionize information technology, but their potential application to cooling technology and magnetocaloric effect (MCE) in a material down to the monolayer limit remain unexplored. Herein, we reveal through multiscale calculations the existence of giant MCE and its strain tunability in monolayer magnets such as CrX_3 (X = F, Cl, Br, I), CrAX (A = O, S, Se; X = F, Cl, Br, I), and Fe_3GeTe_2. The maximum adiabatic temperature change (ΔT_{ad}^{max}), maximum isothermal magnetic entropy change, and specific cooling power in monolayer CrF_3 are found as high as 11 K, 35 μJ m^{-2} K^{-1}, and 3.5 nW cm^{-2} under a magnetic field of 5 T, respectively. A 2% biaxial and 5% *a*-axis uniaxial compressive strain can remarkably increase ΔT_{ad}^{max} of $CrCl_3$ and CrOF by 230% and 37% (up to 15.3 and 6.0 K), respectively. It is found that large net magnetic moment per unit area favors improved MCE. These findings advocate the giant-MCE monolayer magnets, opening new opportunities for magnetic cooling at nanoscale.

1 Introduction

Two-dimensional (2D) magnets, such as $Cr_2Ge_2Te_6$, CrI_3, VSe_2, Fe_3GeTe_2, VI_3 [1–6], have motivated numerous explorations of novel magnetic properties and their applications down to the monolayer limit over the past few years [7–12]. With the additional spin degree of freedom and emergent phenomena in the 2D limit, 2D magnets have shown intriguing prospects in fields such as spin valves [13], magnetic tunnel junctions [14], magnetic random access memory [15, 16], and quantum computing [17, 18]. These applications of 2D magnets favor the development of miniaturized spintronic and magnonic devices [19–22] and could potentially revolutionize the next-generation of information storage/transport technologies [23–26]. Comparatively, the application of 2D magnets in cooling technology has been relatively underdeveloped compared to the tremendous efforts put into exploiting 2D magnets for information technology. Considering the flexibility of 2D magnets and the potential for mechanical deformation, their application in cooling technology is promising.

Cooling technology by using magnetic materials is intrinsically attributed to the magnetocaloric effect (MCE). MCE is a magneto-thermodynamic phenomenon. By exposing magnets to an external magnetic field, a reversible temperature and entropy change could be achieved to result in a targeted cooling or heating. MCE in bulk magnetocaloric materials have been demonstrated to enable highly efficient and environmentally friendly solid-state cooling technology that is a promising alternative to conventional gas-compression refrigerators [27–31]. Despite this, studies on MCE in layered van der Waals (vdW) materials

are still rare. Layered vdW magnets provide a platform for studying the thickness dependent MCE, which have enormous applications in low-dimensional magnetic refrigeration.

Recently, MCE in the bulk counterparts of 2D vdW magnets have been investigated, and the figures of merit for the MCE evaluation (e.g., maximum adiabatic temperature change $\Delta T_{\rm ad}^{\rm max}$, maximum magnetic entropy change $-\Delta S_{\rm M}^{\rm max}$) are reported [32–37]. For instance, by using the heat capacity data at an out-of-plane magnetic field up to 9 T, $\Delta T_{\rm ad}^{\rm max}$ and $-\Delta S_{\rm M}^{\rm max}$ of bulk CrI_3 single crystals are estimated as 2.34 K and 5.65 $\rm J\,kg^{-1}\,K^{-1}$, respectively. In addition, MCE in bulk CrI_3 single crystals is found to be anisotropic [32, 37] and the mechanism of this phenomenon is clarified theoretically, which depends on the anisotropic magnetic susceptibility and magnetization anisotropy [37]. Similarly, for bulk $CrBr_3$ single crystals under an in-plane magnetic field of 5 T, $\Delta T_{\rm ad}^{\rm max}$ and $-\Delta S_{\rm M}^{\rm max}$ are measured as around 2.37 K and 7.2 $\rm J\,kg^{-1}\,K^{-1}$, respectively [33]. Later, bulk $CrCl_3$ are reported to have $-\Delta S_{\rm M}^{\rm max}$ of 14.6 $\rm J\,kg^{-1}\,K^{-1}$ under an in-plane magnetic field of 5 T [34]. Furthermore, a magnetic field of 7 T is shown to induce a large $\Delta T_{\rm ad}^{\rm max}$ of 6.2 K and $-\Delta S_{\rm M}^{\rm max}$ of 19 $\rm J\,kg^{-1}\,K^{-1}$ in bulk $CrCl_3$ [35]. In contrast to bulk CrI_3 [32], MCE in bulk $CrCl_3$ is isotropic [35]. In contrast to typical magnetocaloric materials (such as $La(Fe,Si)_{13}$ family, $Gd_5(Si,Ge)_4$ family, and rare earth compounds) [38], these vdW magnets exhibit superior magnetothermal properties and are suitable for use in low-temperature working environments up to 100 K. Additionally, MCE in magnetic films is widely examined experimentally, but the film is of a thickness around 10^1–10^4 nm [39–41] and is much thicker than a monolayer layer. Thus, most of the current studies are restricted to bulk and film magnets and MCE in monolayer magnets remains to be explored.

In this work, we provide the new insight on the MCE of magnets down to the monolayer limit by a multiscale theoretical approach integrating *ab-initio* calculations, atomistic spin simulations, and magnetocaloric thermodynamics. Specifically, monolayer magnets such as CrX_3 (X = F, Cl, Br, I) and CrAX (A = O, S, Se; X = F, Cl, Br, I) are taken as model systems to explore their MCE. By using the magnetic parameters from *ab-initio* calculations, atomistic spin model simulations are performed to determine the temperature dependent demagnetization curves, from which MCE is evaluated via the Maxwell relations. It is found that MCE indeed remains in these 2D magnets and can be remarkably tuned by strain. More importantly, giant MCE with a $\Delta T_{\rm ad}^{\rm max}$ around 15.3 K is realized in magnets down to the monolayer limit. These results provide theoretical guidance to probe MCE in 2D magnets, and could promote 2D magnets toward applications for cooling or thermal management in compact and miniaturized nanodevices.

2 Results And Discussion

2.1 Strain-tunable magnetic properties

CrX_3 exhibits a rhombohedral lattice (space group $R\bar{3}$), while the atomic arrangement of CrAX shows an orthorhombic structure (space group $Pmmn$). The top and side views of CrX_3 and CrAX structures are shown in Fig 1, in which the associated primitive cells are highlighted with red lines. The optimized lattice parameters are summarized in Table 1, agreeing well with the previous works [42–45]. Exfoliation experiments of CrI_3 [2], $CrBr_3$ [46], CrOCl [47], CrOBr [48], and CrSBr [48] have been carried out to show that the intrinsic ferromagnetism can maintain from the bulk to few-layer or even monolayer thickness. In addition, for certain CrX_3 and CrAX which are not experimentally synthesized yet, their dynamic stability and existence possibility have been confirmed by a suite of theoretical studies [42, 49–51]. The calculated phonon dispersion spectra of CrAX are shown in Fig. S1 (supporting information), proving the dynamic stability of these monolayers.

The magnetic parameters of monolayer CrX_3 and CrAX are recorded in Table 1. Magnetism in these chromium-containing compounds originates from the incompletely filled electrons in d orbitals of Cr ions. The net magnetic moment per primitive cell ($M_{\rm tot}$) is about 6 $\mu_{\rm B}$, whereas the magnetic moment of Cr

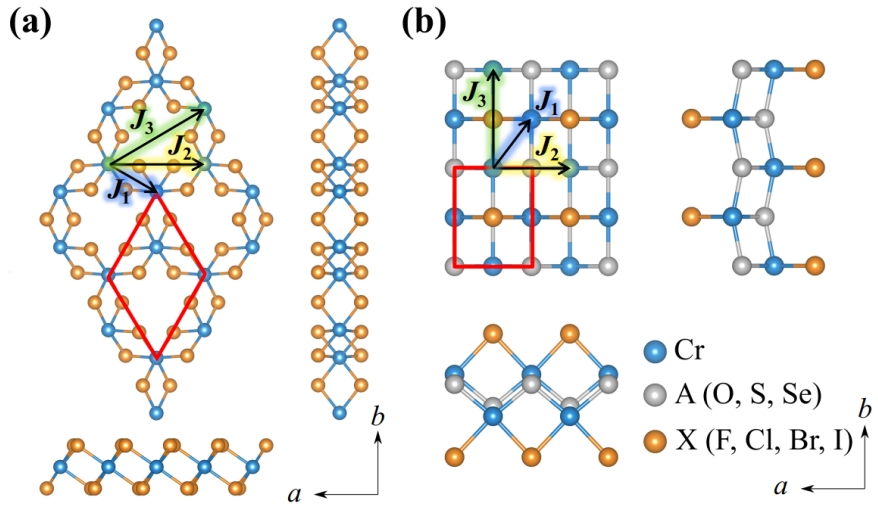


Figure 1: Crystal structures of (a) CrX_3 and (b) CrAX monolayers from the top and side views. The primitive cells of CrX_3 (two Cr and six X atoms) and CrAX (two Cr, two A atoms and two X atoms) have been indicated with red lines. The c axis is perpendicular to the plane composed of a axis and b axis.

atoms (M_{Cr}) is clearly different in these monolayers. Magnetocrystalline anisotropy energy (MAE) the associated easy/hard axis directions are also summarized in Table 1. The monolayers with iodine atoms show strong magnetocrystalline anisotropy. For instance, CrI_3, CrSI, and CrSeI possess a large out-of-plane MAE of 0.745, 1.022, and 0.921 meV, respectively, owing to the strong spin-orbit coupling (SOC) in iodine atoms. The out-of-plane energy of CrF_3, $CrCl_3$, $CrBr_3$, CrI_3, CrOF, CrOCl, and CrSeI is lower than the in-plane one, so an easy axis parallels to c direction holds. Similarly, the easy axis of CrSeCl and CrSeBr is along the a axis. Specially, since the energy in the y direction is lager than that in other directions for

Table 1: Magnetic properties and magnetocaloric parameters including optimized lattice constants (a and b, Å), net magnetic moment per primitive cell (M_{tot}, μ_B), magnetic moment per Cr atom (M_{Cr}, μ_B), net magnetic moment per unit area ($\bar{M}_{tot}$, μA), easy or hard axis direction, magnetocrystalline anisotropy energy (MAE, meV/Cr), the nearest (J_1, meV), next-nearest (J_2, meV), and third-nearest (J_3, meV) neighboring exchange interactions, Curie temperature (T_c, K), maximum magnetic entropy change at 5 T ($-\Delta S_M^{max}$, $\mu J\,m^{-2}\,K^{-1}$) and maximum adiabatic temperature change at 5 T (ΔT_{ad}^{max}, K) for the 13 monolayers.

			Magnetic parameters					Exchange parameters				Magnetocaloric parameters	
Name	a	b	M_{tot}	M_{Cr}	$\bar{M}_{tot}$	easy/hard axis	MAE	J_1	J_2	J_3	T_c	$-\Delta S_M^{max}$	ΔT_{ad}^{max}
CrF_3	5.16		5.82	2.87	233.6	c(E)	0.122	3.81	0.15	-0.03	21	35.04	10.98
$CrCl_3$	6.05		5.68	2.94	166.5	c(E)	0.032	4.21	0.50	-0.28	26	22.55	4.64
$CrBr_3$	6.43		5.72	3.01	147.9	c(E)	0.202	5.81	0.86	-0.33	42	16.07	1.94
CrI_3	7.00		5.74	3.10	125.3	c(E)	0.745	6.54	1.44	-0.35	62	12.98	1.63
CrOF	3.09	3.88	6.02	3.18	466.2	c(E)	0.032	3.6	4.0	7.7	82	31.69	4.37
CrOCl	3.24	3.93	6.02	3.24	438.8	c(E)	0.022	3.5	2.3	7.9	67	31.63	4.75
CrOBr	3.36	3.94	6.05	3.30	423.9	b(H)	0.193	3.3	1.6	7.9	66	32.10	4.00
CrSCl	3.49	4.84	5.94	3.24	325.9	b(H)	0.007	13.6	11.7	3.6	161	12.65	2.11
CrSBr	3.59	4.83	5.95	3.27	318.2	b(H)	0.088	13.5	13.6	5.0	181	11.52	2.09
CrSI	3.76	4.81	5.98	3.32	306.6	b(H)	1.022	12.9	13.5	7.2	203	12.23	2.26
CrSeCl	3.58	5.17	6.02	3.35	301.5	a(E)	0.179	13.6	12.3	-4.6	110	12.89	1.82
CrSeBr	3.68	5.12	6.02	3.37	296.1	a(E)	0.301	13.4	14.9	-2.1	140	12.74	1.97
CrSeI	3.85	5.10	6.05	3.43	285.6	c(E)	0.921	13.6	16.4	1.4	192	11.67	2.15

CrOBr, CrSCl, CrSBr, and CrSI, the b axis is regarded as the hard axis.

The exchange interaction parameters are also listed in Table 1. The positive values of exchange parameters J_1 and J_2 reflect the ferromagnetic coupling in monolayers. J_1 is increased by 2.73 meV in CrX_3 with X varying from F to I, suggesting an enhancement in ferromagnetic coupling. Besides, J_1 and J_2 are one order of magnitude larger than J_3 in CrX_3, and are expected to dominate T_c and the demagnetization behaviors. In contrast, for CrOX, J_3 is even larger than J_1 and J_2. This is possibly attributed to the different atomic structures for forming J_2 and J_3 [52]. J_3 is formed by the super-exchange paths between two neighbor Cr atoms intermediated by an oxygen atom, i.e., Cr–O–Cr in 180°. Whereas, J_2 is formed by two interactions Cr–O–Cr and Cr–X–Cr in 90° [53,54]. Replacement of Cl with Br or I slightly changes J_1 and substantially enlarges J_2 and J_3 in CrSX and CrSeX.

The influence of strain on magnetic properties are further examined. Biaxial strain is applied to CrX_3 and the results are depicted in Fig. 2. The biaxial tensile strain slightly enhances M_{Cr}, but considerably increases the lattice area. Thus the slight increase of M_{Cr} is canceled out and the net magnetic moment per unit area ($\bar{M}_{tot}$) is decreased, as seen in Fig. 2a. MAE of CrI_3 decreases with biaxial strain, while MAE of $CrBr_3$, $CrCl_3$, and CrF_3 increases with it, as shown in Fig. 2b. The impact of strain on exchange parameters J_1 and J_2 is demonstrated in Fig. 2c and 2d, respectively. It is found that J_1 of CrX_3 is reduced by applying biaxial strain in spite of the tensile or compressive types. J_1 of $CrBr_3$, $CrCl_3$, and CrF_3 under –5% compressive biaxial strain becomes negative, confirming that the modulation from ferromagnetic to antiferromagnetic coupling can be realized by applying compressive biaxial strain. J_2 of CrF_3 and others (CrI_3, $CrBr_3$, $CrCl_3$) increases and decreases with the biaxial strain, respectively. The effect of tensile

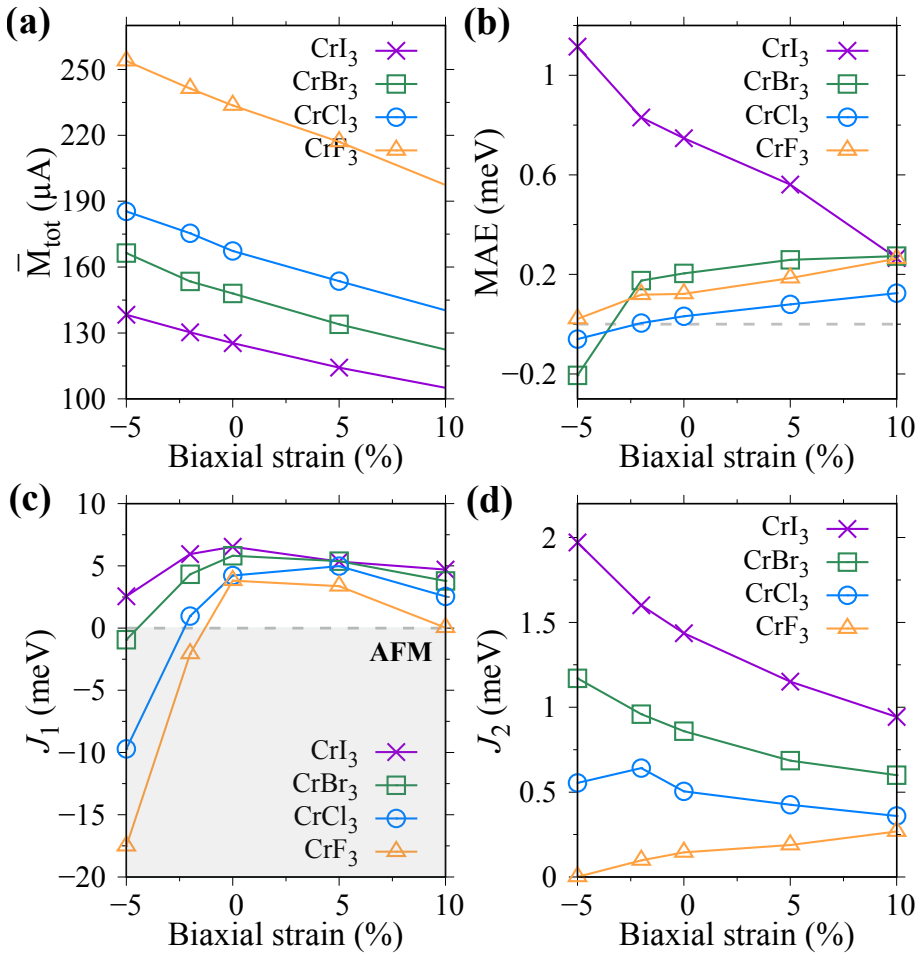


Figure 2: Strain-tunable magnetic properties of CrX_3: (a) net magnetic moment per unit area, (b) MAE, and exchange parameters (c) J_1 and (d) J_2.

and compressive uniaxial strains in CrAX is also investigated and the results are summarized in Figs. S2 and S3. In addition, it is stated that [55, 56] exchange parameters could be affected by finite temperature induced atom displacements. However, as shown in Fig. S4, for 2D magnets whose MCE works at low temperatures, atom displacements are too small to notably affect magnetic properties, indicating the reasonable approximation of applying zero-K magnetic parameters in the classic spin Hamiltonians and the inconspicuous finite-temperature effect on MCE at low temperatures. Nevertheless, further in-depth studies are essential to calculate magnetic properties by considering atom displacements from vibration modes of 2D magnets if elevated temperatures are of interests.

2.2 Demagnetization behavior at finite temperatures

The typical isothermal magnetization curves for CrI_3 and CrOBr at different temperatures are shown in Fig. 3. A striking distinction of saturation magnetization between CrI_3 and CrOBr can be noticed in Fig. 3a and 3b. For CrX_3 and CrAX with similar net magnetic moment, the monolayer with smaller lattice area possesses larger $\bar{M}_{tot}$ and thus higher saturation magnetization at the same temperature. The magnetization curves of other monolayers are shown in Figs. S5–S8.

Figure 3 also indicates the anisotropy of the magnetization curve with respect to the direction of the applied magnetic fields, but the anisotropy is unconspicuous at elevated temperatures. Owing to the hexagonal structures of CrX_3, the demagnetization behavior is almost identical when the magnetic field is applied along a or b axis. The magnetization curves of CrI_3 are hard to saturate under an in-plane magnetic field, while they reach saturation easily under an out-of-plane one, as shown in Fig. 3a. This indicates c as the easy axis at finite temperatures, agreeing with the high out-of-plane MAE of CrI_3 in Table 1. In contrast, as shown in Fig. 3b, CrOBr presents different magnetization curves in all the three crystallographic axes, owing to its in-plane tetragonal structure. Our density functional theory (DFT) calculation with SOC predicts the highest energy with magnetization along b axis (E_b) and thus b as the hardest axis (i.e. $E_b > E_c > E_a$). However, Fig. 3b indicates that magnetization along c axis is even much harder to be demagnetized than that along b axis. This disagreement arises from the competition between the demagnetization energy in the atomistic spin model and the intrinsic MAE from DFT calculations. The minimization of demagnetization energy favors the in-plane alignment of magnetization, thus reducing E_b by 0.201 meV. Since E_b is only slightly lager than E_c ($E_b - E_c \sim 0.193$ meV), this energy reduction is enough to make E_c exceed E_b and thus c as the harder axis.

Similar results are also summarized in Figs. S5-S8 for other monolayers. The hard or easy axis determined by atomistic spin model simulations could differ from that by the DFT calculations. In addition to CrOBr, this phenomena exist as well in $CrCl_3$, CrOF, CrOCl, CrSCl, and CrSBr. The distinction is mainly attributed to the demagnetization energy. Our atomistic spin model includes the demagnetization

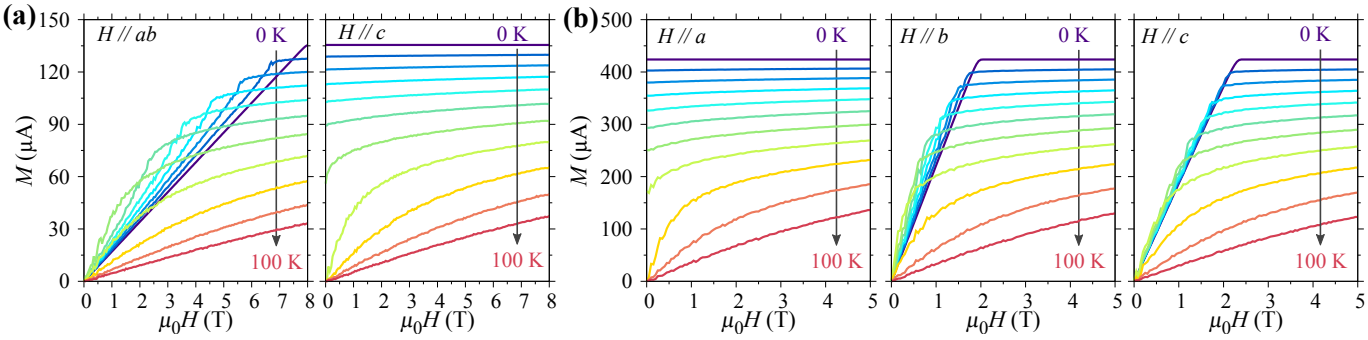


Figure 3: Isothermal magnetization curves of (a) CrI_3 with field up to 8 T and (b) CrOBr with field up to 5 T applied in different directions. The magnetization (M) under different magnetic fields is defined as the net magnetic moment per unit area. The curves are displayed every 10 K.

field and thus the so-called extrinsic shape anisotropy, whereas DFT calculations only give the intrinsic MAE originated from SOC.

2.3 Magnetocaloric effect and its strain tunability

First, we calculate the MCE of bulk CrI_3 and the results are shown in Fig. S9. The calculated results match the experimental measurements [32] very well, confirming the reliability of the MCE calculation methodology that integrates *ab-initio* calculations, Monte-Carlo simulations and magnetocaloric thermodynamics. Moreover, by evaluating MCE in monolayer Fe_3GeTe_2 from the experimental data [4], we find the consistence between experimental results and our theoretical predictions, as well as the indirect experimental evidence for the survive of MCE in monolayer Fe_3GeTe_2, as shown in Fig. S10. The magnetocaloric parameters of monolayers including ΔT_{ad}^{max} and $-\Delta S_M^{max}$ under a magnetic field of 5 T are summarized in Table 1. It is found that CrF_3 outperforms other monolayers, with ΔT_{ad}^{max} and $-\Delta S_M^{max}$ exceeding 10 K and 35 $\mu J\,m^{-2}\,K^{-1}$, respectively. The large $-\Delta S_M^{max}$ of CrF_3 is ascribed to the huge change of magnetization around T_C, as seen in Fig. S5a. The outstanding ΔT_{ad}^{max} of CrF_3 is determined by the smallest density and lowest specific heat capacity at low temperatures. In addition, CrOF and CrOCl also exhibit excellent MCE with ΔT_{ad}^{max} and $-\Delta S_M^{max}$ as high as 4 K and 31 $\mu J\,m^{-2}\,K^{-1}$, respectively. Since CrOF and CrOCl possess significantly large $\bar{M}_{tot}$ and relatively low T_C, their magnetization is more sensitive to the temperature change, thus boosting the $-\Delta S_M$ according to Equation. 2. Besides, CrSX and CrSeX have a

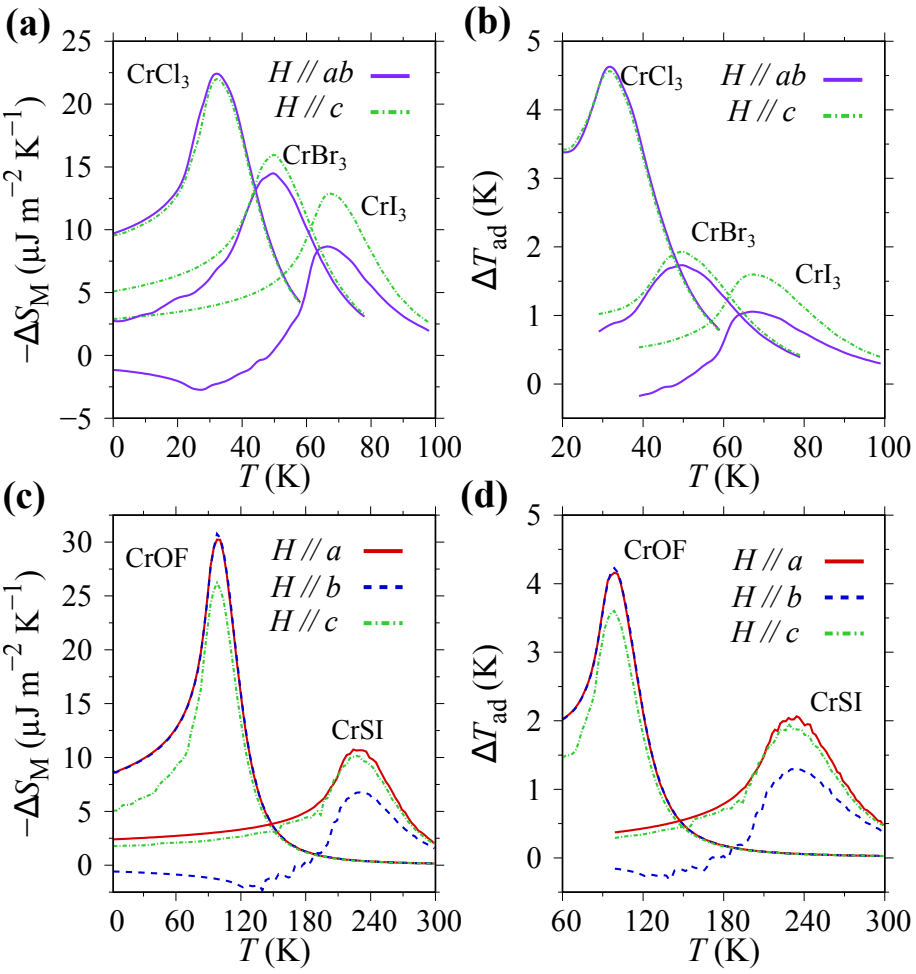


Figure 4: Temperature dependence of negative isothermal magnetic entropy change ($-\Delta S_M$) and the adiabatic temperature change (ΔT_{ad}) under a magnetic field of 5 T applied in different directions. (a), (b) Temperature dependence of $-\Delta S_M$ and ΔT_{ad} for $CrCl_3$, $CrBr_3$, and CrI_3. (c), (d) Temperature dependence of $-\Delta S_M$ and ΔT_{ad} for CrOF and CrSI.

high ΔT_{ad}^{max} and $-\Delta S_M^{max}$ around 4 K and 12 μJ m^{-2} K^{-1}, respectively. Their T_C between 100–200 K makes them potentially applicable in magnetic refrigerants at medium temperatures.

The temperature dependence of $-\Delta S_M$ and ΔT_{ad} under a magnetic field of 5 T applied in different directions is shown in Fig. 4. $-\Delta S_M$ and ΔT_{ad} firstly increase with temperature and then reach their maximum around T_C. This maximum also increases with the applied magnetic field, as shown in Figs. S11-S17. Regardless of the directions of the applied magnetic fields at a fixed temperature, $CrCl_3$ exhibits an almost identical $-\Delta S_M$ and ΔT_{ad}, as shown in Fig. 4a and 4b. This indicates that MCE of $CrCl_3$ is weakly direction dependent, agreeing with the experimental observations on the bulk counterparts [34]. The isotropic MCE behavior could be ascribed to the quite low MAE of $CrCl_3$ in Table 1. In addition, CrOF shows isotropic in-plane MCE that is stronger than the out-of-plane one (Fig. 4c and 4d). The stronger in-plane MCE is mainly owing to the much larger demagnetization energy induced by the highest $\bar{M}_{tot}$ of CrOF and thus much easier rotation of magnetization towards the *ab* plane. On the contrary, due to its large out-of-plane MAE, CrI_3 shows apparently anisotropic MCE. Specifically, $-\Delta S_M^{max}$ and ΔT_{ad}^{max} at 5 T reach 12.98 μJ m^{-2} K^{-1} and 1.63 K along the *c* axis, which are 33% and 35% larger than that in the *ab* plane, respectively. Furthermore, there exists negative *ab*-plane MCE for CrI_3 at low temperatures. This is originated from the competition between the temperature dependence of magnetocrystalline anisotropy and magnetization [32]. For CrI_3 at low temperatures, as the temperature increases, the out-of-plane MAE decreases much more rapidly than the magnetization, leading to a larger in-plane magnetization

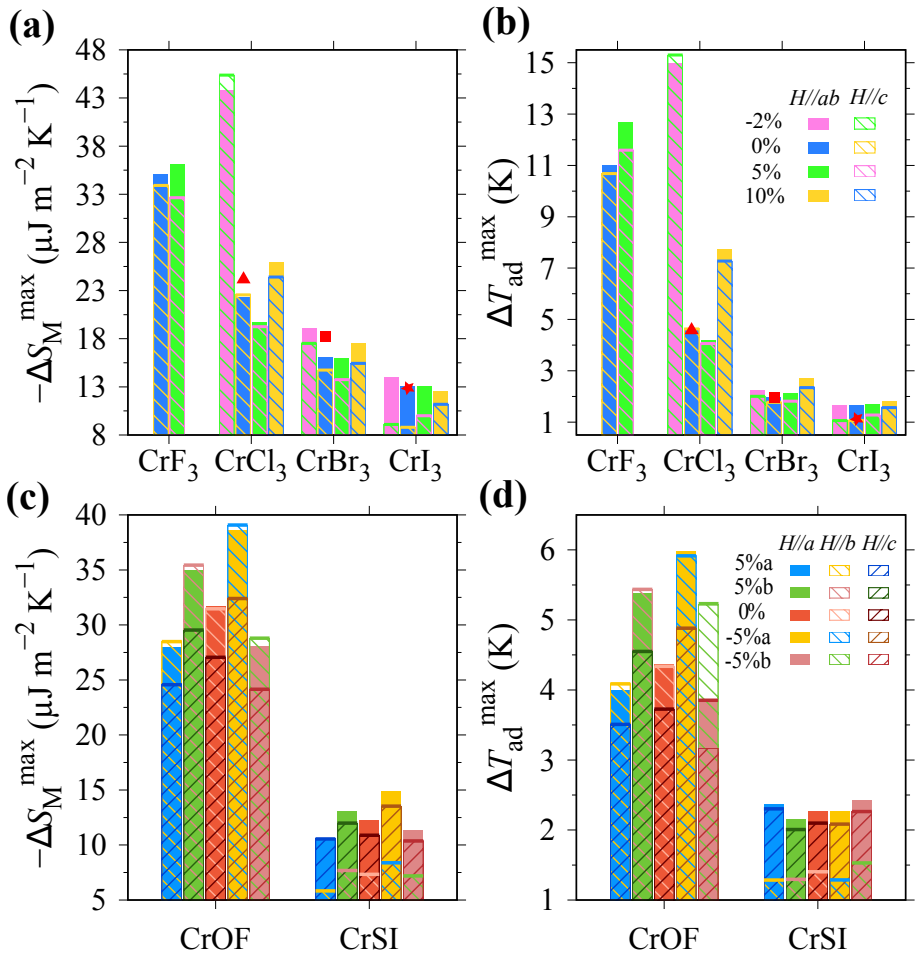


Figure 5: Strain-tunable MCE under a magnetic field of 5 T applied in different directions. (a), (b) $-\Delta S_M^{max}$ and ΔT_{ad}^{max} at –2%, 0%, 5%, and 10% biaxial strain for CrX_3. (c), (d) $-\Delta S_M^{max}$ and ΔT_{ad}^{max} at 5% *a*/*b*-axis tensile and compressive uniaxial strain for CrOF and CrSI. The experimental data of single crystal of bulk $CrCl_3$ [35], $CrBr_3$ [33] and CrI_3 [32] is symbolized by red triangles, squares, and pentagrams, respectively.

(Fig. 3). These explanations are also applicable to CrSI (Fig. 4c and 4d). $-\Delta S_{\mathrm{M}}^{\max}$ and $\Delta T_{\mathrm{ad}}^{\max}$ of these 13 monolayers as a function of magnetic field ranging from 1 to 5 T are summarized in Fig. S18.

To explore the effects of strain on MCE of monolayers, $-\Delta S_{\mathrm{M}}^{\max}$ and $\Delta T_{\mathrm{ad}}^{\max}$ with a magnetic field of 5 T under different strains are shown in Fig. 5. MCE is confirmed to weaken with decreasing layer thickness [40], while ignoring defects and vacancies of monolayers in our calculation allows for the evaluation of ideal magnetocaloric performance. It can be seen from Fig. 5a and 5b that MCE in monolayers of CrX_3 (X = Cl, Br, I) matches well with that in the single-crystal bulk counterparts [32, 33, 35], confirming that MCE can survive in the monolayer limit. It is also found that a considerable enhancement in MCE of $CrCl_3$ is realized by a –2% biaxial compressive strain, with $\Delta T_{\mathrm{ad}}^{\max}$ and $-\Delta S_{\mathrm{M}}^{\max}$ increased by 229% and 101%, respectively (Fig. 5a and 5b). This strain-induced enhancement is primarily a result of increasing $\bar{\mathrm{M}}_{\mathrm{tot}}$ and decreasing T_{C} by the biaxial compressive strain. For MCE in CrOF, a 5% a-axis uniaxial compressive strain is revealed to induce the similar improvements in Fig. 5c and 5d, with $\Delta T_{\mathrm{ad}}^{\max}$ and $-\Delta S_{\mathrm{M}}^{\max}$ of CrOF enhanced by 36.9% and 23.3%, respectively. Although the b-axis uniaxial tensile strain reduces T_{C} as well, the decreased $\bar{\mathrm{M}}_{\mathrm{tot}}$ prevents the significant improvement of MCE.

Since 2D MCE is evaluated in terms of per area rather than per mass or volume, it should be converted to per kilogram before being compared to MCE of typical bulk materials. 1 kg monolayer magnet corresponds to an area in the order of $10^6\,\mathrm{m}^2$ that is unattainable in reality. Here, we take an ideal assumption that 2D magnets could be infinitely large, so the comparison between 2D and bulk is only theoretically feasible. Based on this theoretical and ideal consideration, $-\Delta S_{\mathrm{M}}^{\max}$ and $\Delta T_{\mathrm{ad}}^{\max}$ of monolayers and bulk magnetocaloric materials are compared in Fig. 6. The comparison between the monolayers and classical bulk MCE materials (e.g. conventional 1st and 2nd order materials, inverse 1st order materials) under a low magnetic field of 1 and 2 T [65] is presented in Fig. S19. It can be found from Fig. 6 that in terms of $-\Delta S_{\mathrm{M}}^{\max}$ and $\Delta T_{\mathrm{ad}}^{\max}$, MCE of monolayers is theoretically comparable to that of the bulk materials including typical rare-earth compounds [38, 57, 58], perovskites [59–63], and $La(Fe,Si)_{13}$ [28, 38, 64]. We find that monolayer CrF_3 could work around 20–30 K, which is close to the hydrogen liquefaction temperature. For the state of art of MCE in this temperature range, it is reported that bulk HoB_2 exhibits giant MCE with $-\Delta S_{\mathrm{M}}^{\max}$

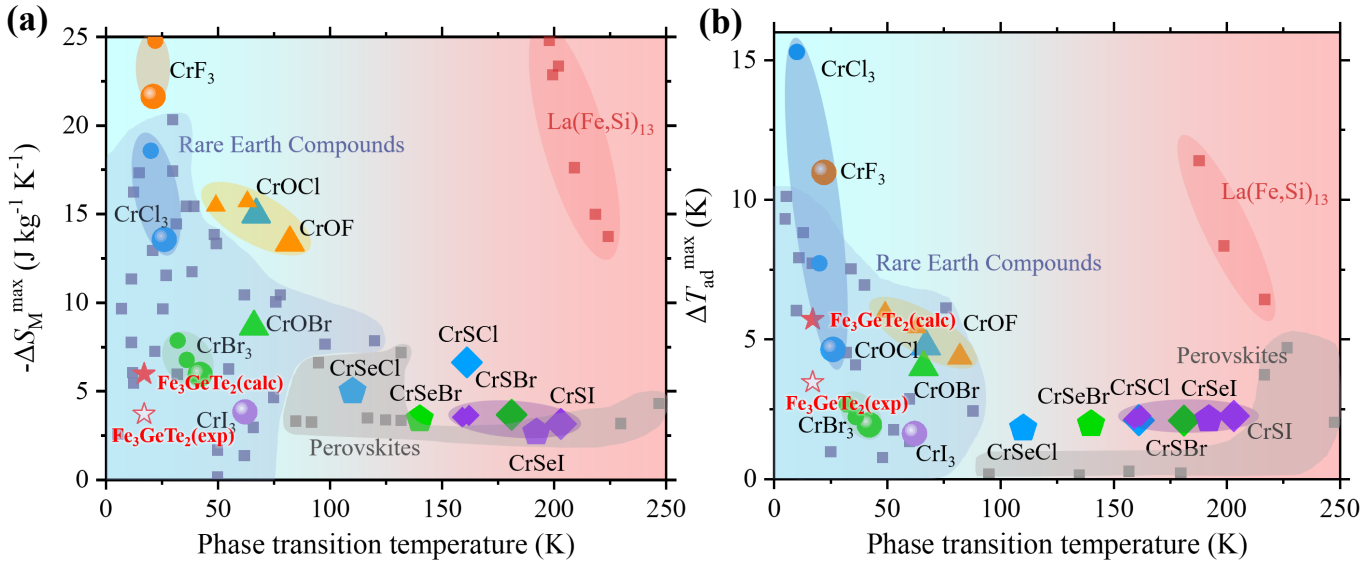


Figure 6: The theoretical and ideal comparison of (a) $-\Delta S_{\mathrm{M}}^{\max}$ and (b) $\Delta T_{\mathrm{ad}}^{\max}$ between the monolayers and classical bulk magnetocaloric materials (i.e., rare earth compounds [38,57,58], perovskites [59–63], and $La(Fe,Si)_{13}$ [28,38,64] at 5 T). CrX_3, CrOX, CrSX, CrSeX and Fe_3GeTe_2 are represented by circles, triangles, rhombuses, pentagons, and pentagrams, respectively. Monolayers containing F, Cl, Br, and I atoms are filled with orange, blue, green, and purple, respectively. The results with strain applied to CrF_3, $CrCl_3$, $CrBr_3$, CrOF, and CrSI are symbolized by smaller points. The experimental and calculated MCE of Fe_3GeTe_2 is from Fig. S10 [4].

SCP (nW cm^{-2})	CrF_3	CrOCl	CrSI
2 T	1.9 @ 25 K	1.7 @ 83 K	0.8 @ 230 K
5 T	3.5 @ 25 K	3.2 @ 83 K	1.2 @ 230 K

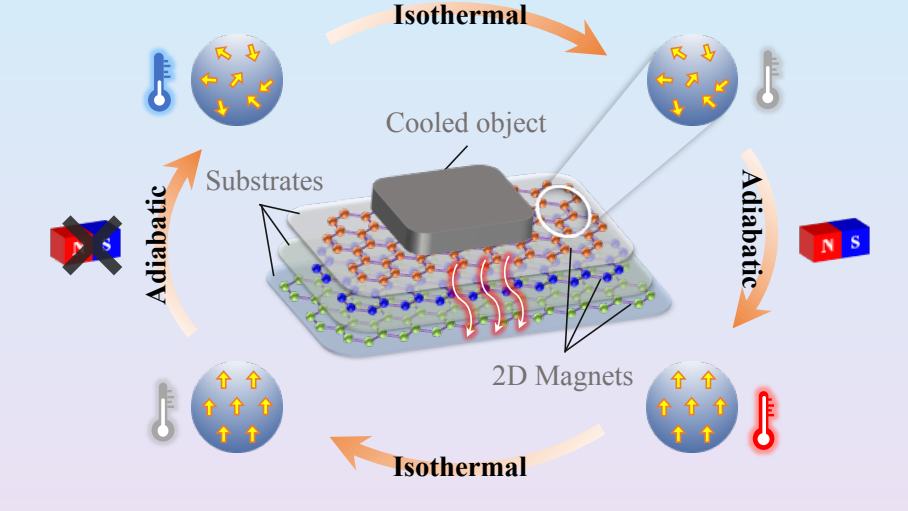


Figure 7: Schematic of refrigeration cycle using MCE of 2D magnets. SCP: specific cooling power.

˜40.1 J kg^{-1} K^{-1} and ΔT_{ad}^{max} ˜12 K for a field change of 5 T [66]. Therefore, it can be found from Fig. 6 that MCE of monolayer CrF_3 ($-\Delta S_M^{max}$ ˜25 J kg^{-1} K^{-1}, ΔT_{ad}^{max} ˜11 K under 5 T) is comparable to that of bulk HoB_2 and rare-earth compounds near the liquid-hydrogen temperature. Perovskites have the advantages of low price, good chemical stability, and widely tunable transition temperature [63,67], while their MCE are unremarkable. The La-Fe-Si compounds with the first-order transition present the large entropy change near room temperature [28, 63], but they suffer from lattice expansion and magnetic thermal hysteresis induced by the first-order transition. In contrast, herein the 2D magnets not only possess giant MCE that is originated from the second-order phase transition without magnetic thermal hysteresis, but also are sufficiently flexible and deformable [68] to allow the further tuning of MCE in 2D magnets by applying large strain. Therefore, mechanically robust 2D magnets could be promising candidates for the cooling of micro/nano devices.

As an illustration, Fig. 7 depicts the possibly magnetic cooling enabled by 2D magnets. As a theoretical and ideal consideration, heat is assumed to be perfectly transferred outward from the cooled object when it contacts 2D magnets under an applied periodic magnetic field. For instance, using 2D CrF_3 as MCE material with an operation frequency of 1 Hz, the ideal specific cooling power (SCP) around 25 K is close to 1.9 nW cm^{-2} at 2 T and 3.5 nW cm^{-2} at 5 T. Under the same condition, the SCP of CrSI around 230 K is 0.8 nW cm^{-2} at 2 T and 1.2 nW cm^{-2} at 5 T. The sequential stacking of 2D magnets with different working temperature windows could provide a cascade refrigeration cycle.

3 Conclusion

In summary, we confirm the survival of giant MCE and its strain tunability of magnets down to the monolayer limit incuding CrX_3 (X = F, Cl, Br, I) and CrAX (A = O, S, Se; X = F, Cl, Br, I) by multiscale simulations. It is found that CrF_3 exhibit excellent magnetocaloric performance at low temperatures owning to the smallest density and lowest specific heat capacity, with ΔT_{ad}^{max} and $-\Delta S_M^{max}$ up to 11 K and 35 μJ m^{-2} K^{-1} under a magnetic field of 5 T, respectively. Meanwhile, CrOF and CrOCl exhibit excellent MCE at medium temperatures with ΔT_{ad}^{max} and $-\Delta S_M^{max}$ as high as 4 K and 31 μJ m^{-2} K^{-1},

respectively. MCE of CrX_3 (X = F, Cl), CrAX (CrOF, CrOCl, CrSCl, CrSBr), and CrSeX is isotropic, in-plane isotropic, and anisotropic, respectively. In addition, compressive strain could effectively enhance MCE by increasing $\bar{M}_{tot}$ and decreasing T_C. Particularly, a 2% biaxial and 5% *a*-axis uniaxial compressive strain can significantly increase ΔT_{ad}^{max} of $CrCl_3$ and CrOF to 15.3 and 6.0 K, respectively. Overall, these findings in our work extend the MCE reaserch to the monolayer limit. Here, we reveal the consistency between experimental and calculated MCE for monolayer Fe_3GeTe2, as well as focus on the theoretical prediction of MCE and the associated mechanism in 2D magnets. The direct measurement of MCE in 2D magnets is currently challenging, but will be feasible as the measuring techniques are advanced. Monolayer magnets with giant and strain-tunable MCE could enable their applications in the cooling of micro/nanoscale space and devices.

4 Experimental Section

DFT Calculations: DFT calculations are performed using *Vienna ab initio simulation page* (VASP) [69,70] within the projector-augmented wave (PAW) method [71, 72]. Exchange-correlation functional adopts Perdew-Burke-Ernzerhof (PBE) type [73] in generalized gradient approximation (GGA). Considering that the calculated results of monolayer CrI_3 without U are more consistent with the experimental values of bulk CrI_3 [74], $U = 0$ eV for CrX_3 is adopted [42]. The calculated magnetic properties of monolayer CrOCl and CrOBr with $U = 7$ eV for Cr are in better agreement with those in their bulk counterparts [45]. The magnetic moment and Curie temperature of monolayer CrSBr calculated with $U = 3$ eV agree well with the experimental measurement [75–77]. As a result, $U = 7$ eV for CrOX and $U = 3$ eV for CrSX and CrSeX are employed. A 15-Å-thick vacuum layer is set to prevent interaction between the periodic lattices along *c* axis. The plane-wave cutoff energy is set to 500 eV and the energy convergence criterion is 10^{-6} eV. The magnetic moment and MAE are evaluated in a primitive cell with a *k*-mesh of $15 \times 15 \times 1$ and $27 \times 21 \times 1$ generated by the Monkhorst-Pack scheme for CrX_3 and CrAX, respectively [78]. MAE is calculated by the difference of total energies with the spin quantization axis aligned along different crystallographic axes. In detail, noncollinear non-self-consistent calculations with SOC are carried out by reading the converged charge densities from the spin-polarized self-consistent calculations. The phonon calculations are performed by the the finite displacement method in a $3 \times 3 \times 1$ supercell [79–81].

In order to calculate the temperature dependent demagnetization curves of 2D magnets, we utilize the atomistic spin model that is based on the classic spin Hamiltonian [82], i.e.,

$$\begin{aligned} H = E_0 - \frac{1}{2}J_1 \sum_N \mathbf{s}_i \cdot \mathbf{s}_j - \frac{1}{2}J_2 \sum_{NN} \mathbf{s}_i \cdot \mathbf{s}_j - \frac{1}{2}J_3 \sum_{NNN} \mathbf{s}_i \cdot \mathbf{s}_j \\ - k_i \sum_i (\mathbf{s}_i \cdot \mathbf{e}_i)^2 - \sum_i \mu_s \mathbf{s}_i \cdot (\mathbf{H_{app}} + \mathbf{H_{dp}}), \end{aligned} \tag{1}$$

in which E_0 is the energy without spin contribution, $\mathbf{s}_i$ the unit vector representing the atomistic spin direction at atom i, k_i the magnetocrytalline anisotropy energy of atom i, and $\mathbf{e}_i$ the easy axis vector. μ_s is the magnetic moment of atom i. $\mathbf{H_{app}}$ and $\mathbf{H_{dp}}$ are the external and dipole magnetic fields, respectively. J_1, J_2, and J_3 are the nearest-neighbour (NN), next-NN, and third-NN exchange interaction parameters, respectively. These exchange parameters are derived by solving equations based on total energies of ferromagnetic and different antiferromagnetic configurations.

Atomistic Spin Simulations: After the parameters in Equation. 1 have been obtained from *ab-initio* calculations, the parameterized atomistic spin model is used to perform simulations by using VAMPIRE [83]. The Monte Carlo method is adopted to acquire T_c. After executing 10,000 steps at each temperature, the system of $50 \times 50 \times 1$ unit cells with in-plane periodic boundary conditions reaches equilibrium. Then a

statistical average is taken over by further 10,000 steps to extract the mean magnetization. The temperature dependent magnetization curves are calculated by using the spin dynamics approach and the Heun integration scheme. The demagnetization field induced by the atomistic spins themselves is also included. The external magnetic field is gradually increased to 8 T with a incremental step of 0.02 T.

Magnetocaloric Thermodynamics: The figures of merit for MCE are related to thermodynamics. The ΔS_{M} can be calculated from the Maxwell relation [84, 85], i.e.,

$$\Delta S_{\mathrm{M}} = \int_0^H \left(\frac{\partial S}{\partial H}\right)_T \mathrm{d}H = \mu_0 \int_0^H \left(\frac{\partial M}{\partial T}\right)_H \mathrm{d}H, \tag{2}$$

where S is entropy, M is magnetization, and μ_0 is vacuum permeability. The degree of disorder in the magnetic moment distribution decreases as the magnetic field increases. So ΔS_{M} turns to a negative value. Thus, usually $-\Delta S_{\mathrm{M}}$ is taken as one of the features to measure MCE. Similarly, ΔT_{ad} could demonstrate MCE directly, which can be represented as

$$\Delta T_{\mathrm{ad}} = -\mu_0 \int_0^H \frac{T}{\rho c_{\mathrm{p}}} \left(\frac{\partial S}{\partial H}\right)_T \mathrm{d}H = -\mu_0 \int_0^H \frac{T}{\rho c_{\mathrm{p}}} \left(\frac{\partial M}{\partial T}\right)_H \mathrm{d}H, \tag{3}$$

where ρ is the density, and c_{p} is the specific heat capacity which is acquired by phonon calculations.

Supporting Information
Supporting Information is available from the Wiley Online Library or from the author.

Acknowledgements
The authors acknowledge the support from the National Natural Science Foundation of China (12272173, 11902150), the 15th Thousand Youth Talents Program of China, the Research Fund of State Key Laboratory of Mechanics and Control of Mechanical Structures (MCMS-I-0419G01 and MCMS-I-0421K01), the Fundamental Research Funds for the Central Universities, a project Funded by the Priority Academic Program Development of Jiangsu Higher Education Institutions, the European Research Council (ERC) under the European Unions Horizon 2020 research and innovation programme (No 743116), the German Research Foundation (DFG YI 165/1-1 and DFG XU 121/7-1).

Conflict of Interest
The authors declare no conflict of interest.

References

[1] C. Gong, L. Li, Z. Li, H. Ji, A. Stern, Y. Xia, T. Cao, W. Bao, C. Wang, Y. Wang, et al., *Nature* **2017**, *546*, 7657 265.

[2] B. Huang, G. Clark, E. Navarro-Moratalla, D. R. Klein, R. Cheng, K. L. Seyler, D. Zhong, E. Schmidgall, M. A. McGuire, D. H. Cobden, et al., *Nature* **2017**, *546*, 7657 270.

[3] M. Bonilla, S. Kolekar, Y. Ma, H. C. Diaz, V. Kalappattil, R. Das, T. Eggers, H. R. Gutierrez, M. H. Phan, M. Batzill, *Nature Nanotechnology* **2018**, *13*, 4 289.

[4] Y. Deng, Y. Yu, Y. Song, J. Zhang, N. Z. Wang, Z. Sun, Y. Yi, Y. Z. Wu, S. Wu, J. Zhu, J. Wang, X. H. Chen, Y. Zhang, *Nature* **2018**, *563*, 7729 94.

[5] C. Tan, J. Lee, S.-G. Jung, T. Park, S. Albarakati, J. Partridge, M. R. Field, D. G. McCulloch, L. Wang, C. Lee, *Nature Communications* **2018**, *9*, 1 1554.

[6] T. Kong, K. Stolze, E. I. Timmons, J. Tao, D. Ni, S. Guo, Z. Yang, R. Prozorov, R. J. Cava, *Advanced Materials* **2019**, *31*, 17 1808074.

[7] J. L. Lado, J. Fernández-Rossier, *2D Materials* **2017**, *4*, 3 035002.

[8] S. Chen, C. Huang, H. Sun, J. Ding, P. Jena, E. Kan, *The Journal of Physical Chemistry C* **2019**, *123*, 29 17987.

[9] M. Pizzochero, R. Yadav, O. V. Yazyev, *2D Materials* **2020**, *7*, 3 035005.

[10] G. Lin, X. Luo, F. Chen, J. Yan, J. Gao, Y. Sun, W. Tong, P. Tong, W. Lu, Z. Sheng, et al., *Applied Physics Letters* **2018**, *112*, 7 072405.

[11] B. Huang, G. Clark, D. R. Klein, D. MacNeill, E. Navarro-Moratalla, K. L. Seyler, N. Wilson, M. A. McGuire, D. H. Cobden, D. Xiao, et al., *Nature Nanotechnology* **2018**, *13*, 7 544.

[12] B. Niu, T. Su, B. A. Francisco, S. Ghosh, F. Kargar, X. Huang, M. Lohmann, J. Li, Y. Xu, T. Taniguchi, et al., *Nano Letters* **2019**, *20*, 1 553.

[13] H. Wang, J. Qi, X. Qian, *Applied Physics Letters* **2020**, *117*, 8 083102.

[14] K. Watanabe, B. Jinnai, S. Fukami, H. Sato, H. Ohno, *Nature Communications* **2018**, *9*, 1 663.

[15] X. Hou, H. Chen, Z. Zhang, S. Wang, P. Zhou, *Advanced Electronic Materials* **2019**, *5*, 9 1800944.

[16] Z. Zhang, Z. Wang, T. Shi, C. Bi, F. Rao, Y. Cai, Q. Liu, H. Wu, P. Zhou, *InfoMat* **2020**, *2*, 2 261.

[17] H. Liu, J. T. Sun, M. Liu, S. Meng, *Journal of Physical Chemistry Letters* **2018**, *9*, 23 6709.

[18] A. J. Littlejohn, Z. Li, Z. Lu, X. Sun, P. Nawarat, Y. Wang, Y. Li, T. Wang, Y. Chen, L. Zhang, H. Li, K. Kisslinger, S. Shi, J. Shi, A. Raeliarijaona, W. Shi, H. Terrones, K. M. Lewis, M. Washington, T. M. Lu, G. C. Wang, *ACS Applied Nano Materials* **2019**, *2*, 6 3684.

[19] A. V. Chumak, V. I. Vasyuchka, A. A. Serga, B. Hillebrands, *Nature Physics* **2015**, *11*, 6 453.

[20] D. MacNeill, G. M. Stiehl, M. H. Guimaraes, R. A. Buhrman, J. Park, D. C. Ralph, *Nature Physics* **2016**, *13*, 3 300.

[21] A. V. Sadovnikov, C. S. Davies, V. V. Kruglyak, D. V. Romanenko, S. V. Grishin, E. N. Beginin, Y. P. Sharaevskii, S. A. Nikitov, *Physical Review B* **2017**, *96* 060401.

[22] W. Zhang, P. K. J. Wong, R. Zhu, A. T. S. Wee, *InfoMat* **2019**, *1*, 4 479.

[23] K. S. Burch, D. Mandrus, J. G. Park, *Nature* **2018**, *563*, 7729 47.

[24] T. Song, X. Cai, M. W. Y. Tu, X. Zhang, B. Huang, N. P. Wilson, K. L. Seyler, L. Zhu, T. Taniguchi, K. Watanabe, M. A. McGuire, D. H. Cobden, D. Xiao, W. Yao, X. Xu, *Science* **2018**, *360*, 6394 1214.

[25] R. Frisenda, E. Navarro-Moratalla, P. Gant, D. Pérez De Lara, P. Jarillo-Herrero, R. V. Gorbachev, A. Castellanos-Gomez, *Chemical Society Reviews* **2018**, *47*, 1 53.

[26] M. Gibertini, M. Koperski, A. F. Morpurgo, K. S. Novoselov, *Nature Nanotechnology* **2019**, *14*, 5 408.

[27] A. M. Omer, *Renewable and Sustainable Energy Reviews* **2008**, *12*, 9 2265.

[28] B. Shen, J. Sun, F. Hu, H. Zhang, Z. Cheng, *Advanced Materials* **2009**, *21*, 45 4545.

[29] O. Gutfleisch, M. A. Willard, E. Brück, C. H. Chen, S. G. Sankar, J. P. Liu, *Advanced Materials* **2011**, *23*, 7 821.

[30] O. Gutfleisch, T. Gottschall, M. Fries, D. Benke, I. Radulov, K. P. Skokov, H. Wende, M. Gruner, M. Acet, P. Entel, et al., *Philosophical Transactions of the Royal Society A: Mathematical, Physical and Engineering Sciences* **2016**, *374*, 2074 20150308.

[31] F. Li, M. Li, X. Xu, Z. Yang, H. Xu, C. Jia, K. Li, J. He, B. Li, H. Wang, *Nature Communications* **2020**, *11*, 1 4190.

[32] Y. Liu, C. Petrovic, *Physical Review B* **2018**, *97*, 17 174418.

[33] X. Yu, X. Zhang, Q. Shi, S. Tian, H. Lei, K. Xu, H. Hosono, *Frontiers of Physics* **2019**, *14*, 4 6.

[34] Y. Liu, C. Petrovic, *Physical Review B* **2020**, *102*, 1 014424.

[35] S. Mondal, A. Midya, M. M. Patidar, V. Ganesan, P. Mandal, *Applied Physics Letters* **2020**, *117*, 9 092405.

[36] Y. Liu, M. Abeykoon, C. Petrovic, et al., *Physical Review Research* **2020**, *2*, 1 013013.

[37] H. B. Tran, H. Momida, Y. ichiro Matsushita, K. Shirai, T. Oguchi, *Acta Materialia* **2022**, *231* 117851.

[38] V. Franco, J. Blázquez, J. Ipus, J. Law, L. Moreno-Ramírez, A. Conde, *Progress in Materials Science* **2018**, *93* 112.

[39] N. Teichert, D. Kucza, O. Yildirim, E. Yuzuak, I. Dincer, A. Behler, B. Weise, L. Helmich, A. Boehnke, S. Klimova, A. Waske, Y. Elerman, A. Hütten, *Physical Review B* **2015**, *91* 184405.

[40] J. Döntgen, J. Rudolph, T. Gottschall, O. Gutfleisch, S. Salomon, A. Ludwig, D. Hägele, *Applied Physics Letters* **2015**, *106*, 3 032408.

[41] D. Nguyen Ba, Y. Zheng, L. Becerra, M. Marangolo, M. Almanza, M. LoBue, *Physical Review Applied* **2021**, *15* 064045.

[42] W.-B. Zhang, Q. Qu, P. Zhu, C.-H. Lam, *Journal of Materials Chemistry C* **2015**, *3* 12457.

[43] C. Xu, J. Zhang, Z. Guo, S. Zhang, X. Yuan, L. Wang, *Journal of Physics: Condensed Matter* **2021**, *33*, 19 195804.

[44] Y. Guo, Y. Zhang, S. Yuan, B. Wang, J. Wang, *Nanoscale* **2018**, *10*, 37 18036.

[45] R. Han, Z. Jiang, Y. Yan, *Journal of Physical Chemistry C* **2020**, *124*, 14 7956.

[46] Z. Zhang, J. Shang, C. Jiang, A. Rasmita, W. Gao, T. Yu, *Nano Letters* **2019**, *19*, 5 3138.

[47] T. Zhang, Y. Wang, H. Li, F. Zhong, J. Shi, M. Wu, Z. Sun, W. Shen, B. Wei, W. Hu, X. Liu, L. Huang, C. Hu, Z. Wang, C. Jiang, S. Yang, Q. M. Zhang, Z. Qu, *ACS Nano* **2019**, *13*, 10 11353.

[48] K. Lee, A. H. Dismukes, E. J. Telford, R. A. Wiscons, J. Wang, X. Xu, C. Nuckolls, C. R. Dean, X. Roy, X. Zhu, *Nano Letters* **2021**, *21*, 8 3511.

[49] J. Liu, Q. Sun, Y. Kawazoe, P. Jena, *Physical Chemistry Chemical Physics* **2016**, *18* 8777.

[50] Q.-Y. Rong, A.-M. Hu, X.-H. Zhang, L.-L. Wang, W.-Z. Xiao, *Journal of Magnetism and Magnetic Materials* **2020**, *515* 167310.

[51] J. Xiao, D. Legut, W. Luo, H. Guo, X. Liu, R. Zhang, Q. Zhang, *Physical Review B* **2020**, *101*, 1 014431.

[52] T. Xiao, G. Wang, Y. Liao, *Chemical Physics* **2018**, *513*, April 182.

[53] F. Zhang, Y. C. Kong, R. Pang, L. Hu, P. L. Gong, X. Q. Shi, Z. K. Tang, *New Journal of Physics* **2019**, *21*, 5.

[54] X. Jiang, Q. Liu, J. Xing, N. Liu, Y. Guo, Z. Liu, J. Zhao, *Applied Physics Reviews* **2021**, *8*, 3 031305.

[55] B. Sadhukhan, A. Bergman, Y. O. Kvashnin, J. Hellsvik, A. Delin, *Physical Review B* **2022**, *105*, 10 104418.

[56] D. Staros, G. Hu, J. Tiihonen, R. Nanguneri, J. Krogel, M. C. Bennett, O. Heinonen, P. Ganesh, B. Rubenstein, *The Journal of Chemical Physics* **2022**, *156*, 1 014707.

[57] A. Midya, S. N. Das, P. Mandal, S. Pandya, V. Ganesan, *Physical Review B* **2011**, *84* 235127.

[58] Y. Zhang, *Journal of Alloys and Compounds* **2019**, *787* 1173.

[59] M.-H. Phan, S.-C. Yu, N. H. Hur, Y.-H. Jeong, *Journal of Applied Physics* **2004**, *96*, 2 1154.

[60] M. Patra, K. De, S. Majumdar, S. Giri, *Applied Physics Letters* **2009**, *94* 092506.

[61] A. M. Aliev, A. B. Batdalov, L. N. Khanov, *Applied Physics Letters* **2018**, *112*, 14 142407.

[62] A. G. Gamzatov, A. M. Aliev, P. D. Yen, L. Khanov, K. X. Hau, T. D. Thanh, N. T. Dung, S. C. Yu, *Journal of Applied Physics* **2018**, *124*, 18 183902.

[63] N. R. Ram, M. Prakash, U. Naresh, N. S. Kumar, T. S. Sarmash, T. Subbarao, R. J. Kumar, G. R. Kumar, K. C. B. Naidu, *Journal of Superconductivity and Novel Magnetism* **2018**, *31*, 7 1971.

[64] L. Jia, J. R. Sun, J. Shen, Q. Y. Dong, J. D. Zou, B. Gao, T. Y. Zhao, H. W. Zhang, F. X. Hu, B. G. Shen, *Journal of Applied Physics* **2009**, *105*, 7 07A924.

[65] T. Gottschall, K. P. Skokov, M. Fries, A. Taubel, I. Radulov, F. Scheibel, D. Benke, S. Riegg, O. Gutfleisch, *Advanced Energy Materials* **2019**, *9*, 34 1970130.

[66] P. B. de Castro, K. Terashima, T. D. Yamamoto, Z. Hou, S. Iwasaki, R. Matsumoto, S. Adachi, Y. Saito, P. Song, H. Takeya, Y. Takano, *NPG Asia Materials* **2020**, *12*, 1 1.

[67] N. A. Zarkevich, V. I. Zverev, *Crystals* **2020**, *10*, 9 815.

[68] F. Cantos-Prieto, A. Falin, M. Alliati, D. Qian, R. Zhang, T. Tao, M. R. Barnett, E. J. G. Santos, L. H. Li, E. Navarro-Moratalla, *Nano Letters* **2021**, *21*, 8 3379.

[69] G. Kresse, J. Furthmüller, *Physical Review B* **1996**, *54* 11169.

[70] G. Kresse, D. Joubert, *Physical Review B* **1999**, *59* 1758.

[71] P. E. Blöchl, *Physical Review B* **1994**, *50* 17953.

[72] G. Kresse, J. Furthmüller, *Computational Materials Science* **1996**, *6*, 1 15.

[73] J. P. Perdew, K. Burke, M. Ernzerhof, *Physical Review Letters* **1996**, *77* 3865.

[74] J. F. Dillon, C. E. Olson, *Journal of Applied Physics* **1965**, *36*, 3 1259.

[75] S. A. López-Paz, Z. Guguchia, V. Y. Pomjakushin, C. Witteveen, A. Cervellino, H. Luetkens, N. Casati, A. F. Morpurgo, F. O. von Rohr, *Nature Communications* **2022**, *13*, 1 1.

[76] N. P. Wilson, K. Lee, J. Cenker, K. Xie, A. H. Dismukes, E. J. Telford, J. Fonseca, S. Sivakumar, C. Dean, T. Cao, X. Roy, X. Xu, X. Zhu, *Nature Materials* **2021**, *20*, 12 1657.

[77] A. Avsar, *Nature Materials* **2022**, *21*, 7 731.

[78] H. J. Monkhorst, J. D. Pack, *Physical Review B* **1976**, *13* 5188.

[79] A. Togo, I. Tanaka, *Scripta Materialia* **2015**, *108* 1359.

[80] L. Chaput, A. Togo, I. Tanaka, G. Hug, *Physical Review B* **2011**, *84* 094302.

[81] A. Togo, L. Chaput, I. Tanaka, G. Hug, *Physical Review B* **2010**, *81* 174301.

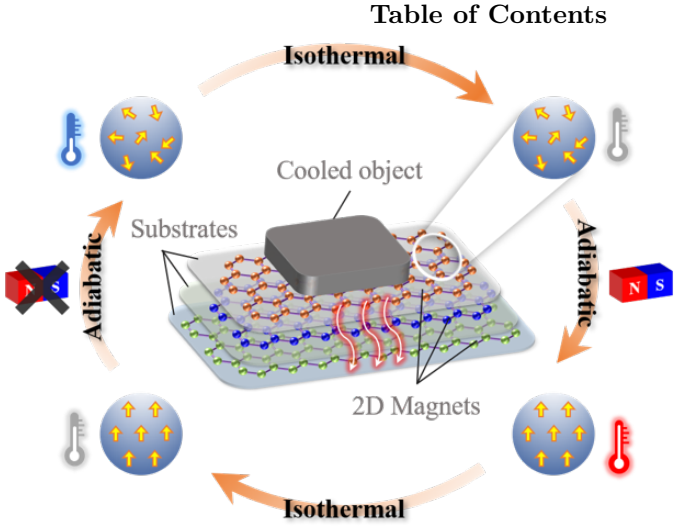
[82] B. Skubic, J. Hellsvik, L. Nordström, O. Eriksson, *Journal of Physics: Condensed Matter* **2008**, *20*, 31 315203.

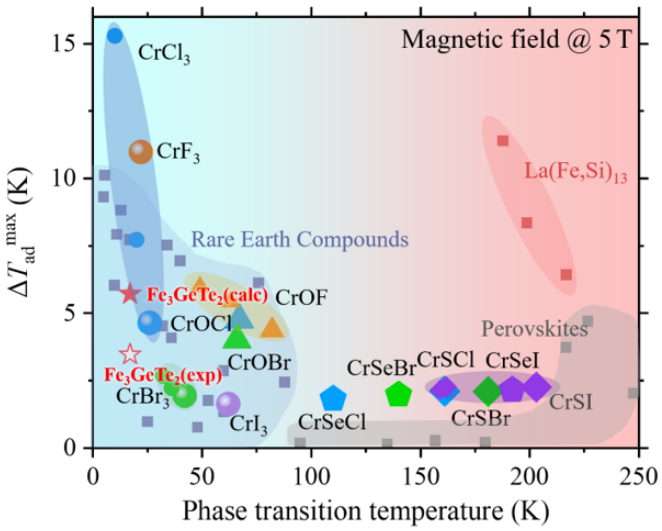
[83] R. F. Evans, W. J. Fan, P. Chureemart, T. A. Ostler, M. O. Ellis, R. W. Chantrell, *Journal of Physics: Condensed Matter* **2014**, *26*, 10 103202.

[84] V. K. Pecharsky, K. A. Gschneidner, *Journal of Applied Physics* **1999**, *86*, 1 565.

[85] K. A. Gschneidner, V. K. Pecharsky, *Annual Review of Materials Science* **2000**, *30*, 1 387.

Table of Contents





The existence of giant magnetocaloric effect (MCE) and its strain tunability in monolayer magnets such as CrX_3 (X = F, Cl, Br, I), CrAX (A = O, S, Se; X = F, Cl, Br, I), and Fe_3GeTe_2 are revealed through multiscale calculations. MCE of 2D magnets is theoretically comparable to that of bulk materials and can be remarkably tuned by strain. In particular, CrF_3 possesses the state-of-the-art MCE at low temperatures. These findings advocate the giant-MCE monolayer magnets, opening new opportunities for magnetic cooling at nanoscale.

Supplementary information

Giant magnetocaloric effect in magnets down to the monolayer limit

Weiwei He,[†] Yan Yin,[†] Qihua Gong,[*,†] Richard F. L. Evans,[‡] Oliver Gutfleisch,[¶] Baixiang Xu,[¶] Min Yi,[*,†] and Wanlin Guo[*,†]

[†]*State Key Lab of Mechanics and Control of Mechanical Structures & Key Lab for Intelligent Nano Materials and Devices of Ministry of Education & Institute for Frontier Science, Nanjing University of Aeronautics and Astronautics (NUAA), Nanjing 210016, China*

[‡]*Department of Physics, The University of York, York YO105DD, United Kingdom*

[¶]*Institute of Materials Science, Technische Universität Darmstadt, Darmstadt 64287, Germany*

E-mail: gongqihua@nuaa.edu.cn; yimin@nuaa.edu.cn; wlguo@nuaa.edu.cn

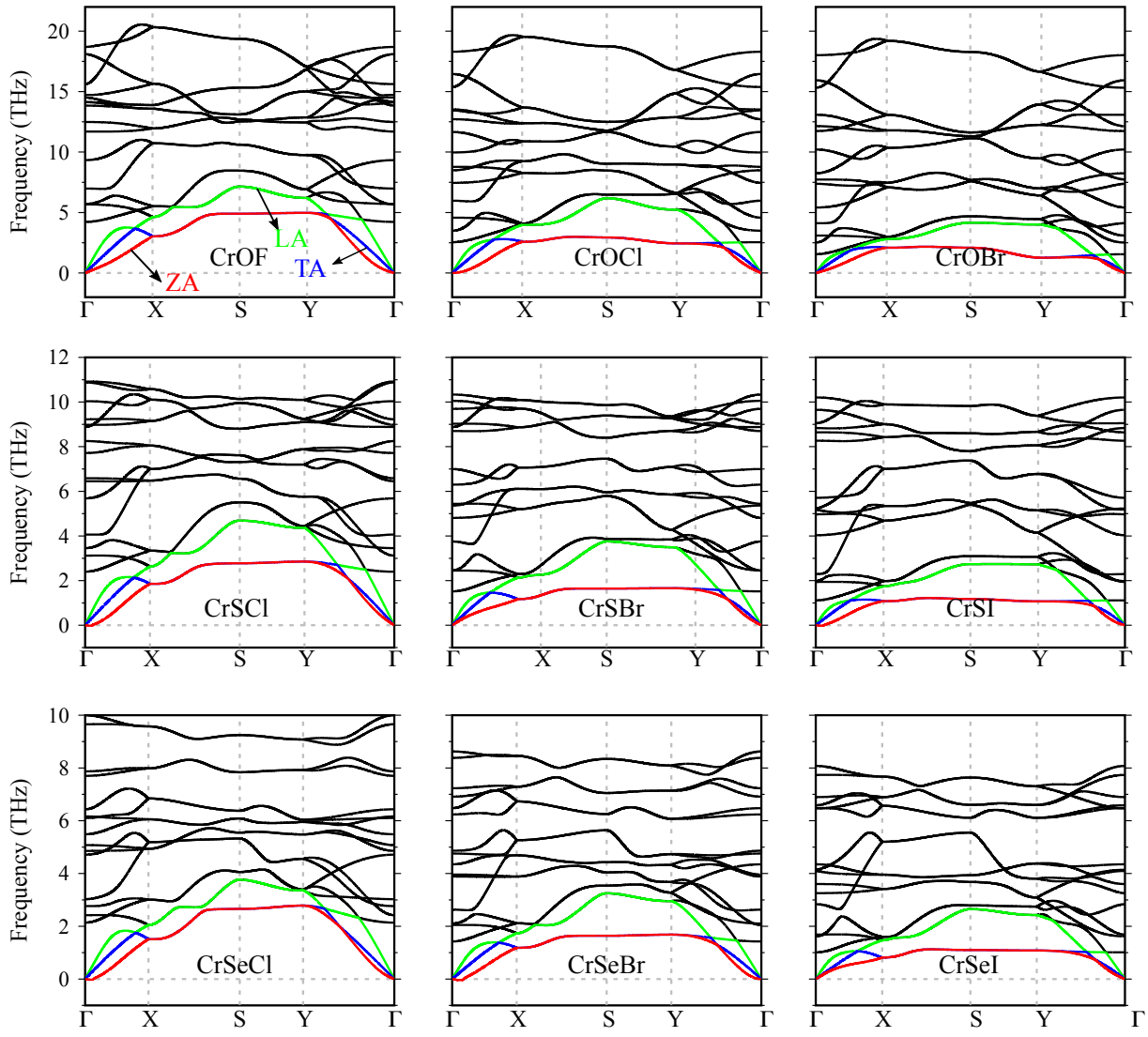


Fig. S1. Phonon dispersion spectra of 2D CrAX.

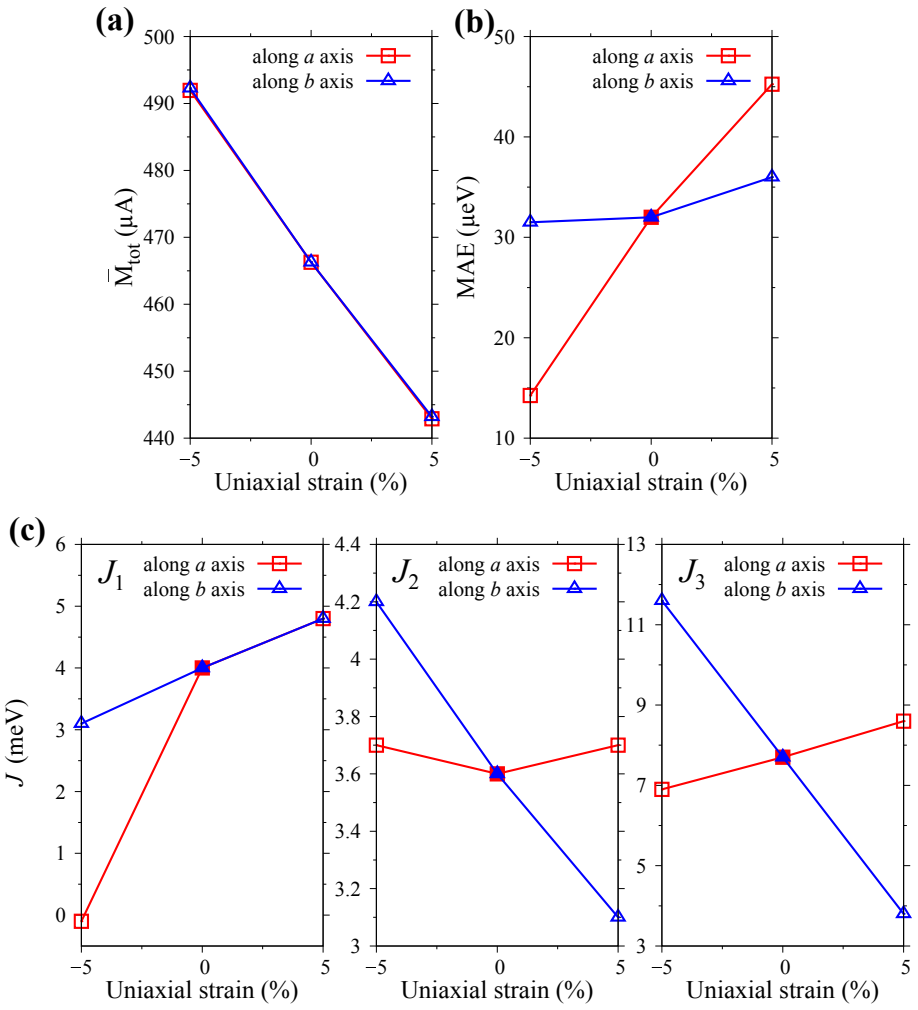


Fig. S2. Strain-tunable magnetic properties of CrOF: (a) net magnetic moment per unit area, (b) MAE, and (c) exchange parameters J_1, J_2 and J_3.

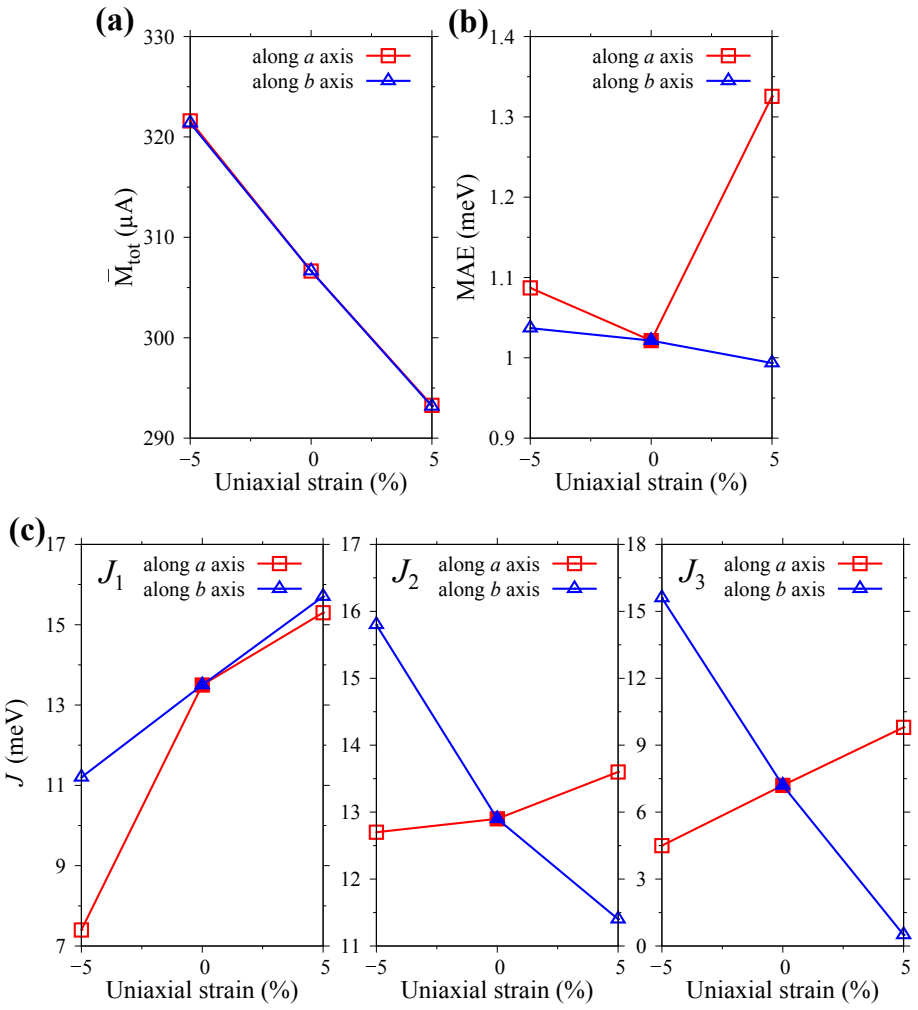


Fig. S3. Strain-tunable magnetic properties of CrSI: (a) net magnetic moment per unit area, (b) MAE, and (c) exchange parameters J_1, J_2 and J_3.

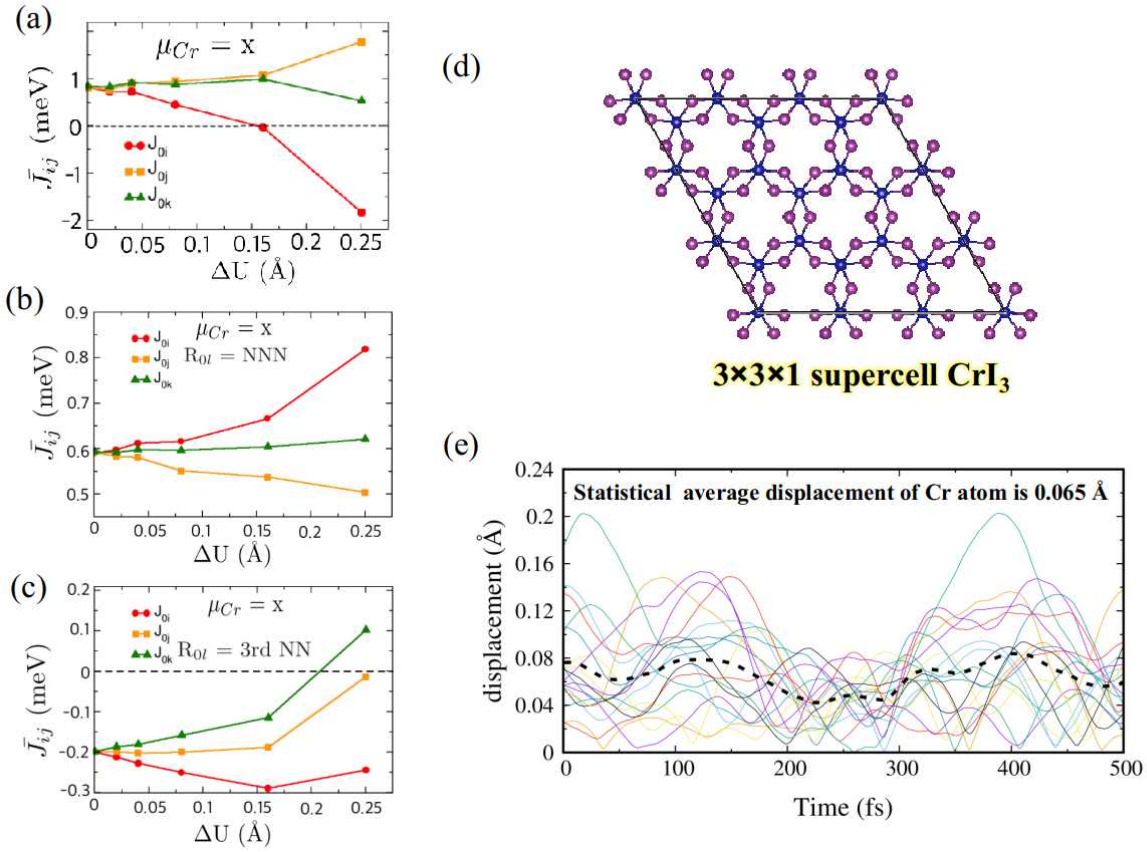


Fig. S4. Temperature effect in exchange interaction. The effect of displacement on (a) the nearest-neighbor (NN), (b) next NN, and (c) third NN exchange interaction of monolayer CrI_3 (figures from ref[1]). (d) The calculated structure of the 3×3×1 supercell CrI_3 and (e)the calculated displacement of each time step at 60 K by *ab-initio* molecular dynamics simulations. The average displacement of Cr is estimated as 0.065 Å. As previously discussed,[1,2] exchange parameters could be affected by finite temperature induced atom displacements and are found only slightly changed when the Cr displacement is less than 0.1 Å.[1] However, the critical temperature of CrI_3 is around 60 K, at which Cr atoms are averagely displaced by about 0.065 Å (d, e). This small displacement will not notably affect the magnetic properties, indicating the reasonable approximation of applying zero-K magnetic parameters in the classic spin Hamiltonians. Thus, the finite-temperature effect on MCE at low temperatures should be inconspicuous. Nevertheless, further in-depth studies are required to calculate the magnetic properties by considering the atom displacements from the vibration modes of 2D magnets if elevated temperatures are of interests.

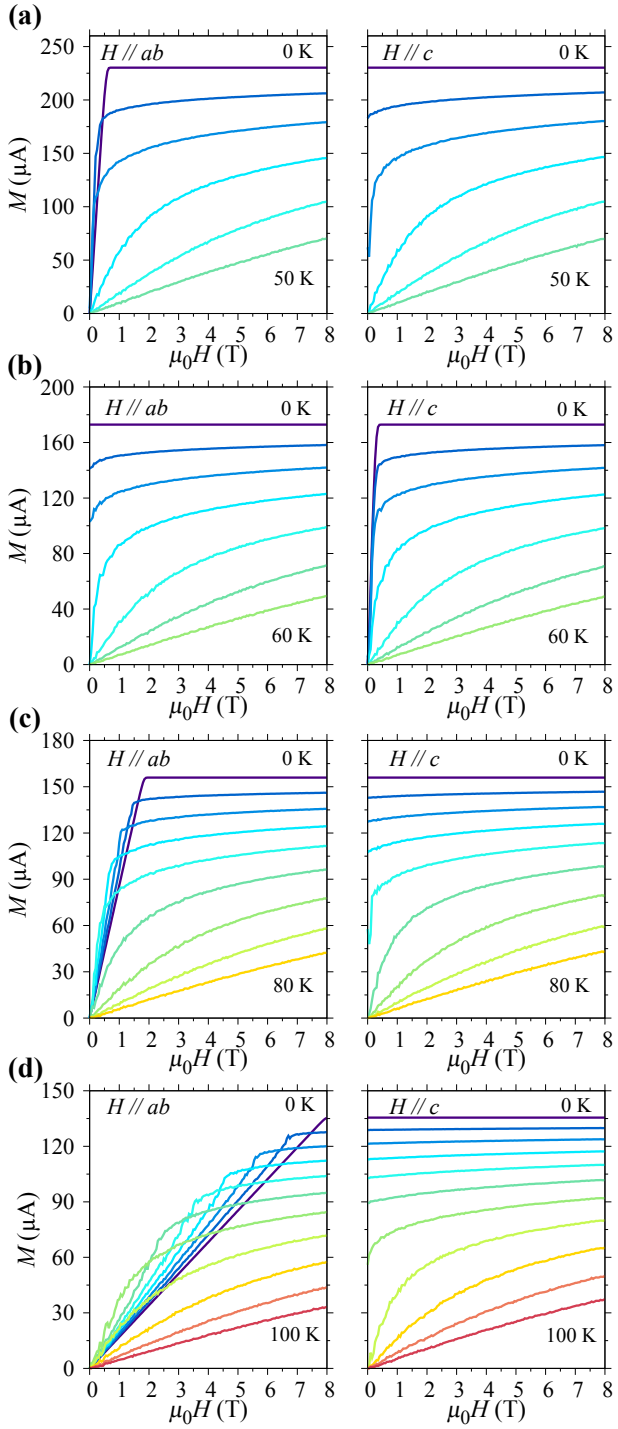


Fig. S5. Isothermal magnetization curves with field up to 8 T applied in the *ab* plane (left) and along the *c* axis (right) for (a) CrF_3, (b) $CrCl_3$, (c) $CrBr_3$, and (d) CrI_3. The curves are displayed every 10 K.

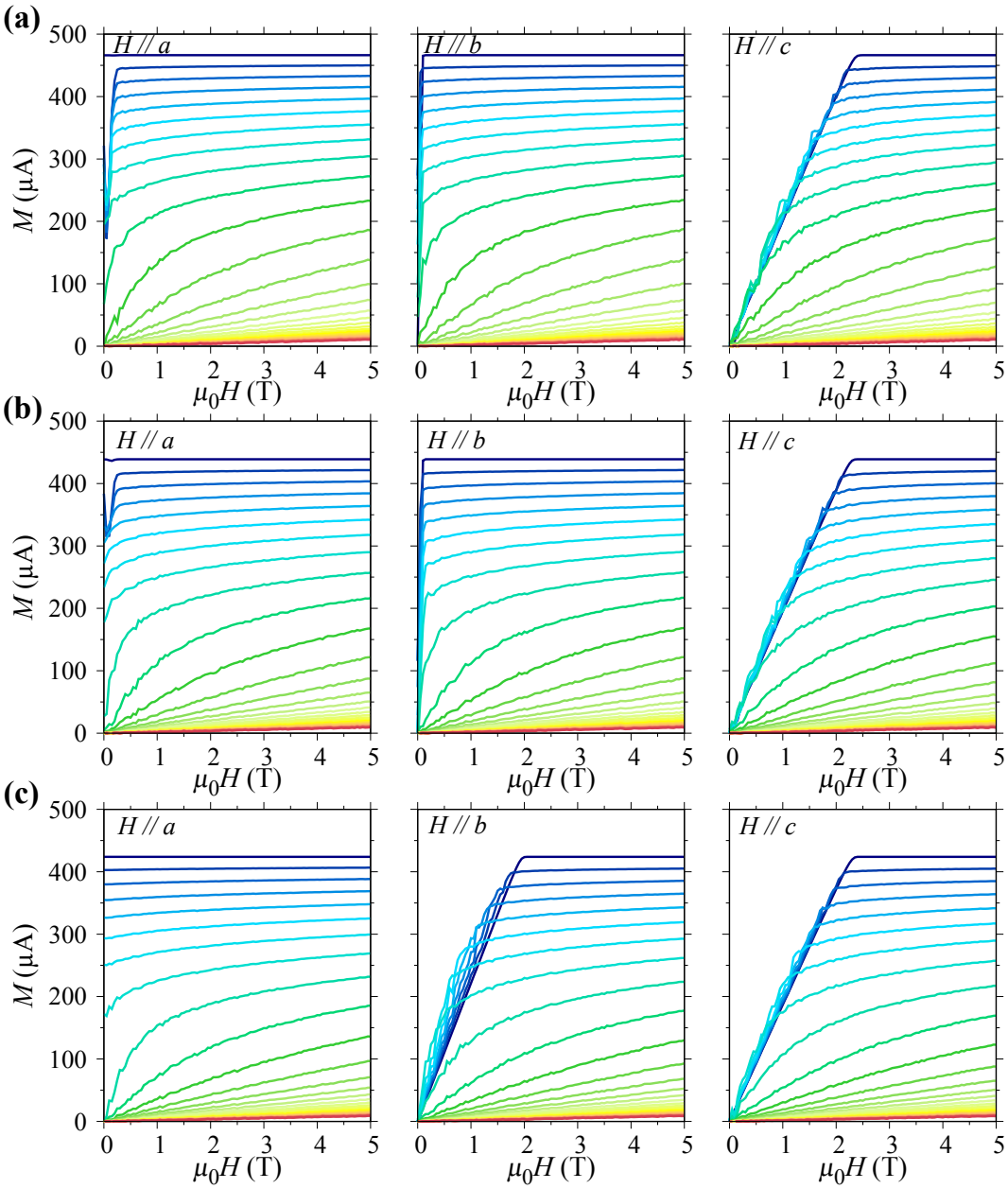


Fig. S6. Isothermal magnetization curves with field up to 5 T applied along the a axis (left), b axis (middle), and c axis (right) for (a) CrOF, (b) CrOCl, and (c) CrOBr. The curves are displayed every 10 K with a temperature range from 0 K to 300 K.

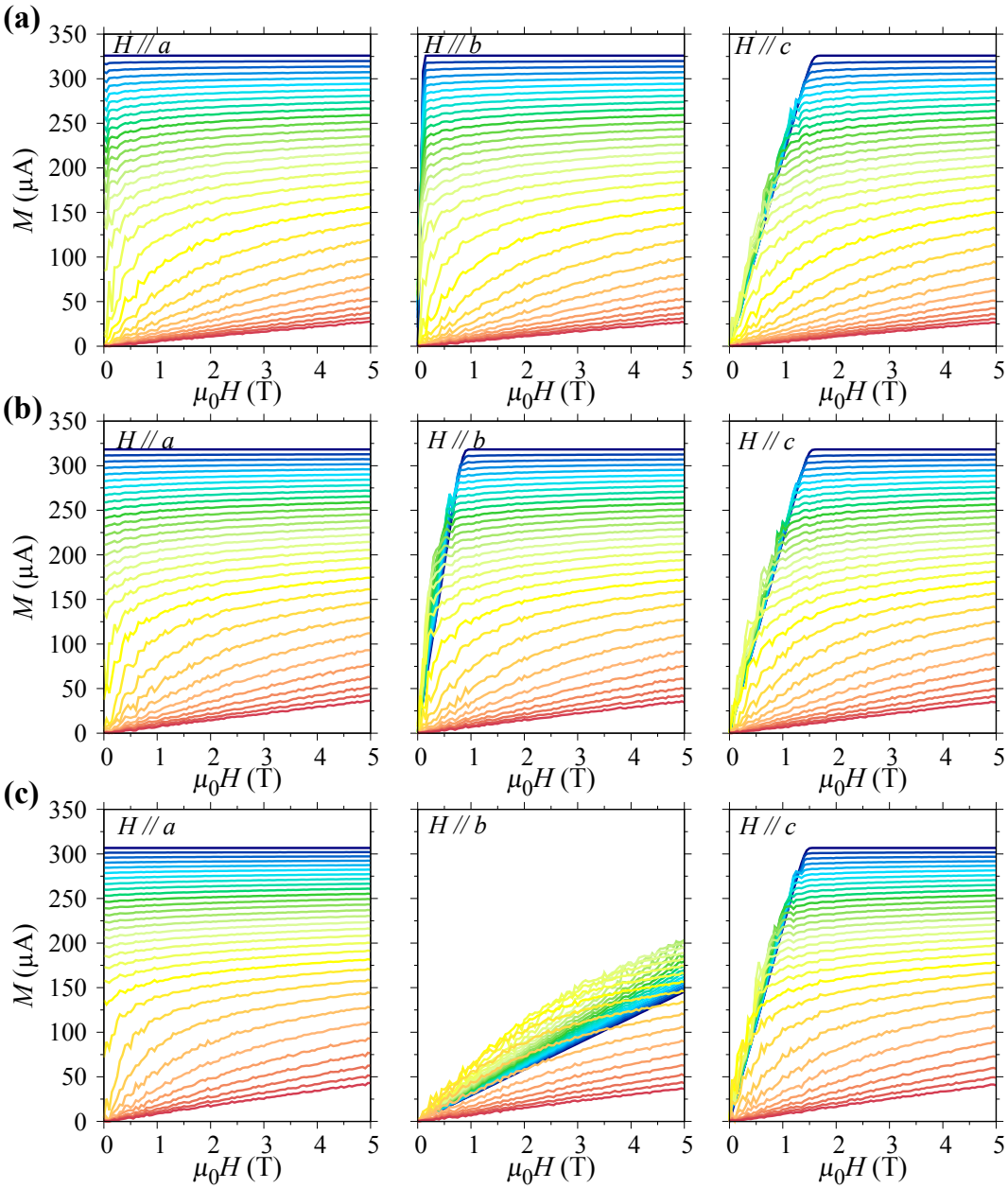


Fig. S7. Isothermal magnetization curves with field up to 5 T applied along the a axis (left), b axis (middle) and c axis (right) for (a) CrSCl, (b) CrSBr, and (c) CrSI. The curves are displayed every 10 K with a temperature range from 0 K to 300 K.

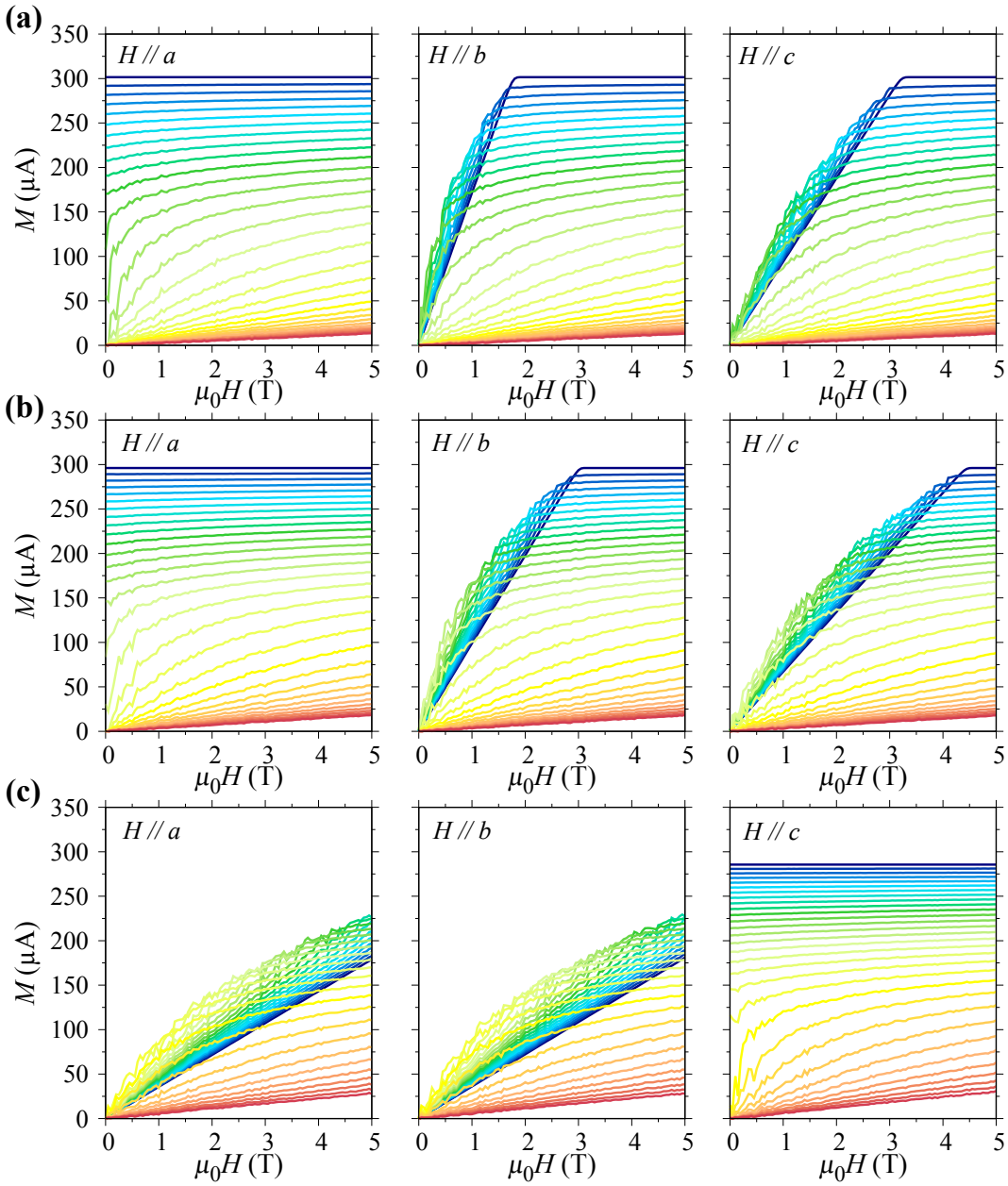


Fig. S8. Isothermal magnetization curves with field up to 5 T applied along the a axis (left), b axis (middle) and c axis (right) for (a) CrSeCl, (b) CrSeBr, and (c) CrSeI. The curves are displayed every 10 K with a temperature range from 0 K to 300 K.

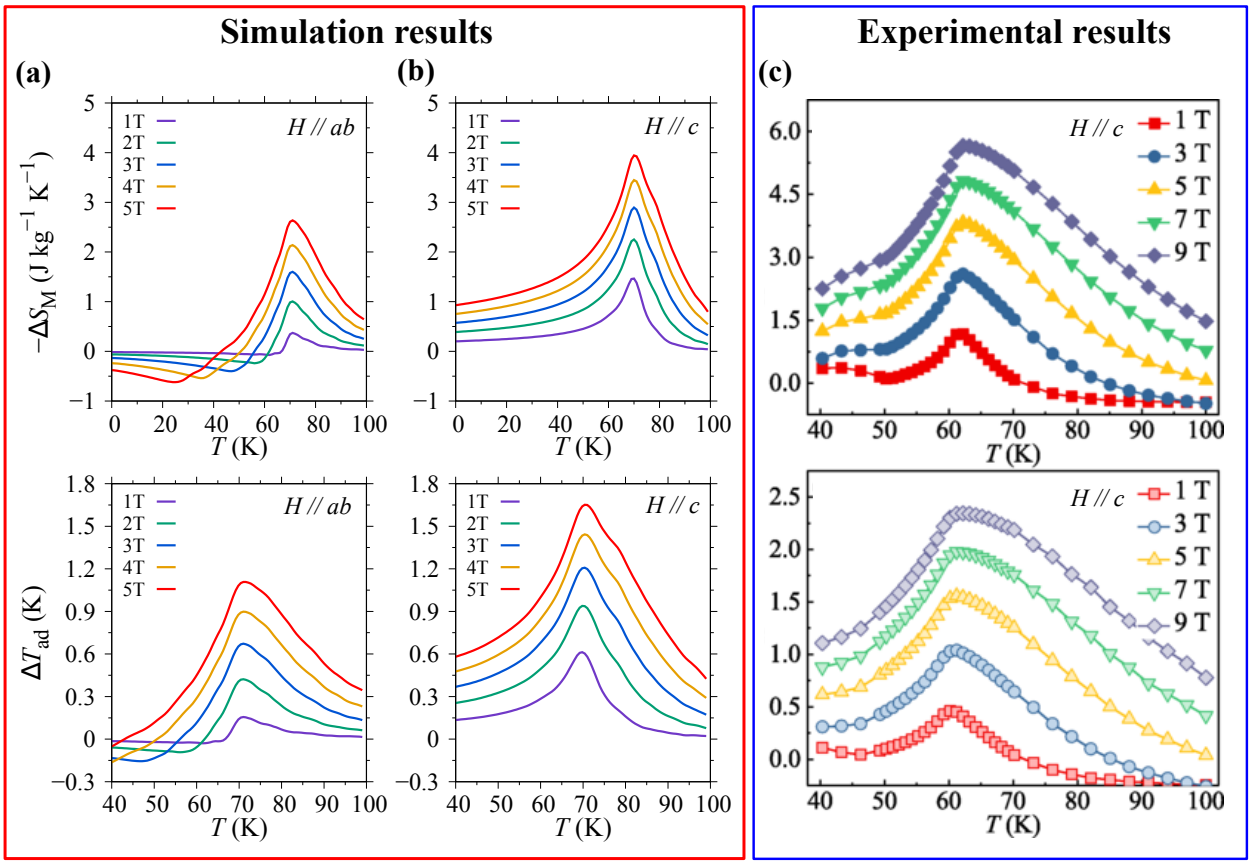


Fig. S9. Simulation and experimental results for MCE of bulk CrI_3. Simulated temperature-dependent $-\Delta S_M$ (top) and ΔT_{ad} (bottom) for (a) $H \parallel ab$ and (b) $H \parallel c$ in different magnetic fields, respectively. Experimental temperature-dependent $-\Delta S_M$ (top) and ΔT_{ad} (bottom) for (c) $H \parallel c$ in different magnetic fields. Experimental curves in (c) are from ref.[3]

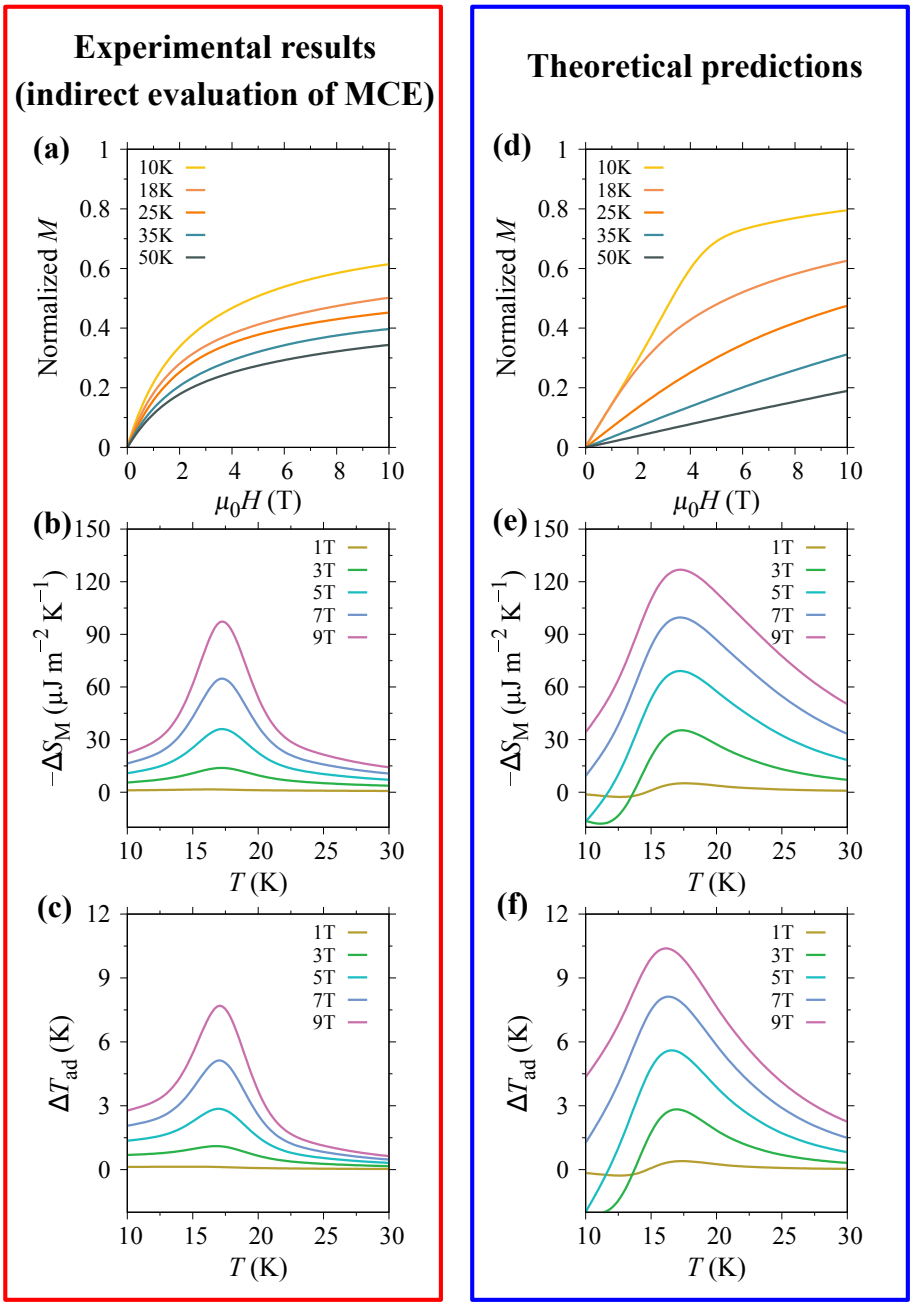


Fig. S10. MCE of monolayer Fe_3GeTe_2 from experimental results and theoretical predictions. Temperature-dependent M-H curves: (a) experiment; (d) prediction. $-\Delta S_M$ curves under different magnetic fields: (b) experiment; (e) prediction. ΔT_{ad} curves under different magnetic fields: (c) experiment; (f) prediction. The experimental data of monolayer Fe_3GeTe_2 are from ref.[4]

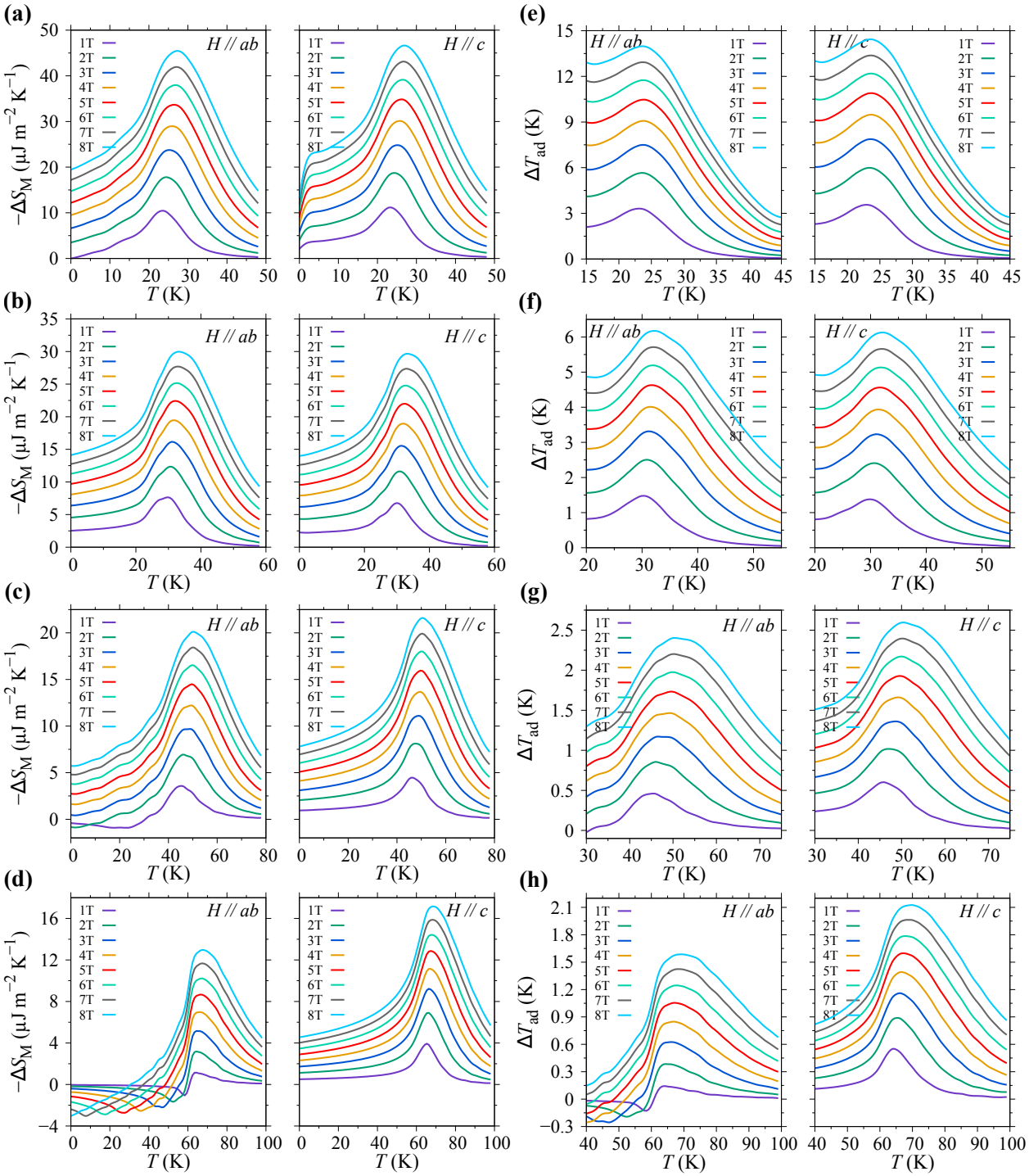


Fig. S11. Temperature dependences of (a-d) $-\Delta S_{\mathrm{M}}$ and (e-h) ΔT_{ad} of monolayer CrX_3 for $H \parallel ab$ and $H \parallel c$ in different magnetic fields, respectively. (a) and (e) are for CrF_3, (b) and (f) are for $CrCl_3$, (c) and (g) are for $CrBr_3$, (d) and (h) are for CrI_3.

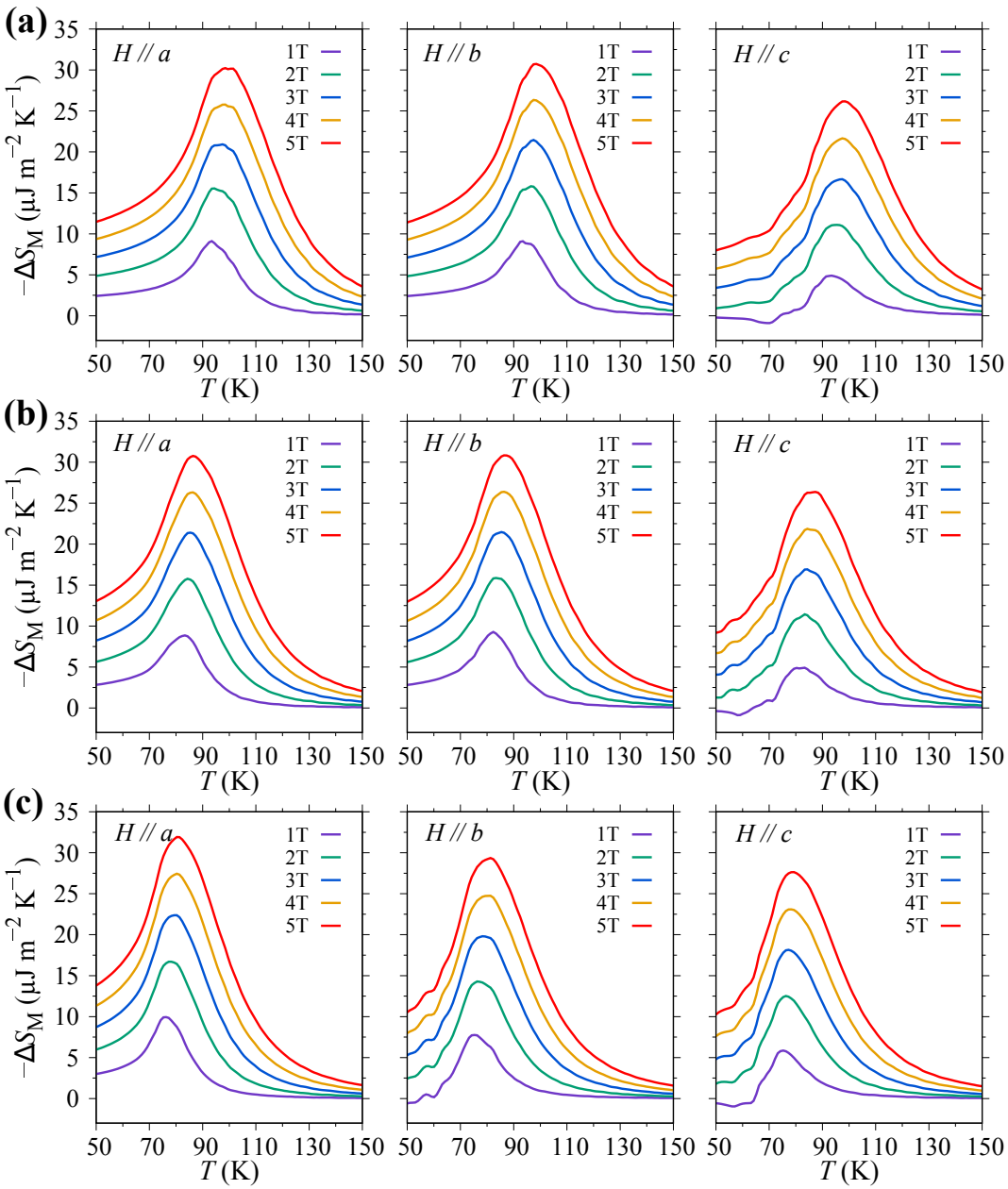


Fig. S12. Temperature dependences of $-\Delta S_{\mathrm{M}}$ of monolayer (a) CrOF, (b) CrOCl and (c) CrOBr for $H \parallel a$, $H \parallel b$, and $H \parallel c$ in different magnetic fields, respectively.

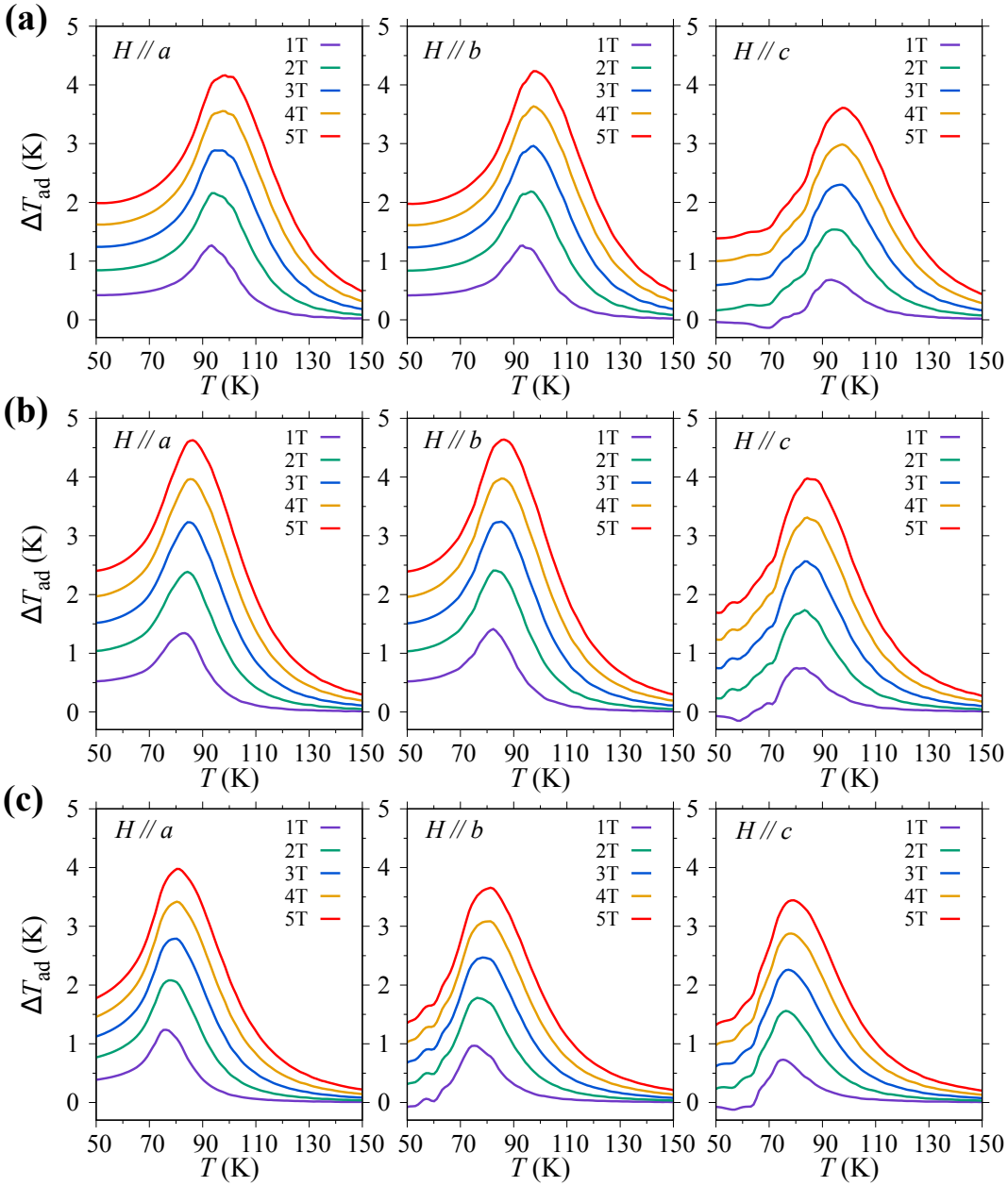


Fig. S13. Temperature dependences of ΔT_{ad} of monolayer (a) CrOF, (b) CrOCl and (c) CrOBr for $H \parallel a$, $H \parallel b$, and $H \parallel c$ in different magnetic fields, respectively.

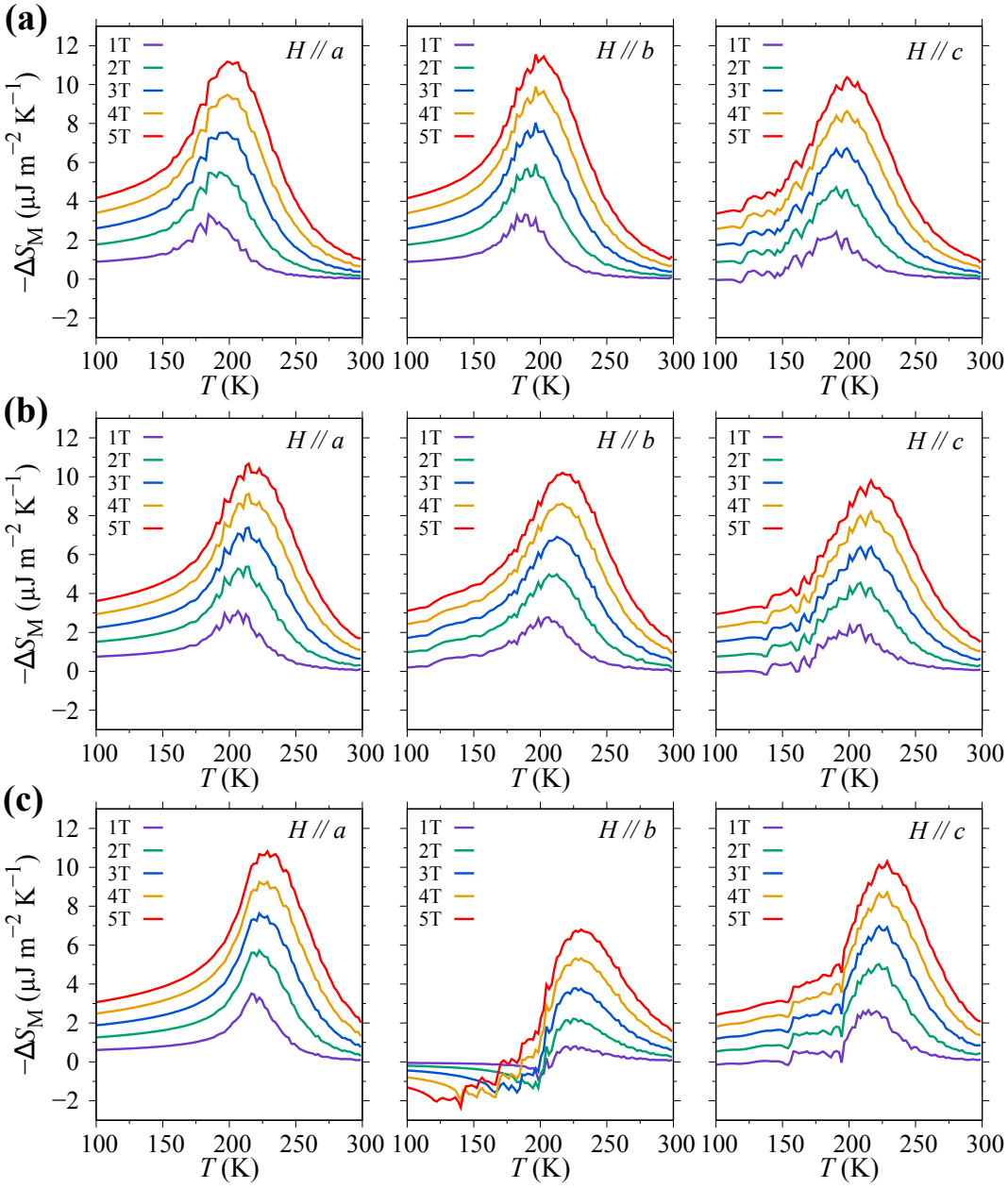


Fig. S14. Temperature dependences of $-\Delta S_{\mathrm{M}}$ of monolayer (a) CrSCl, (b) CrSBr and (c) CrSI for $H \parallel a$, $H \parallel b$, and $H \parallel c$ in different magnetic fields, respectively.

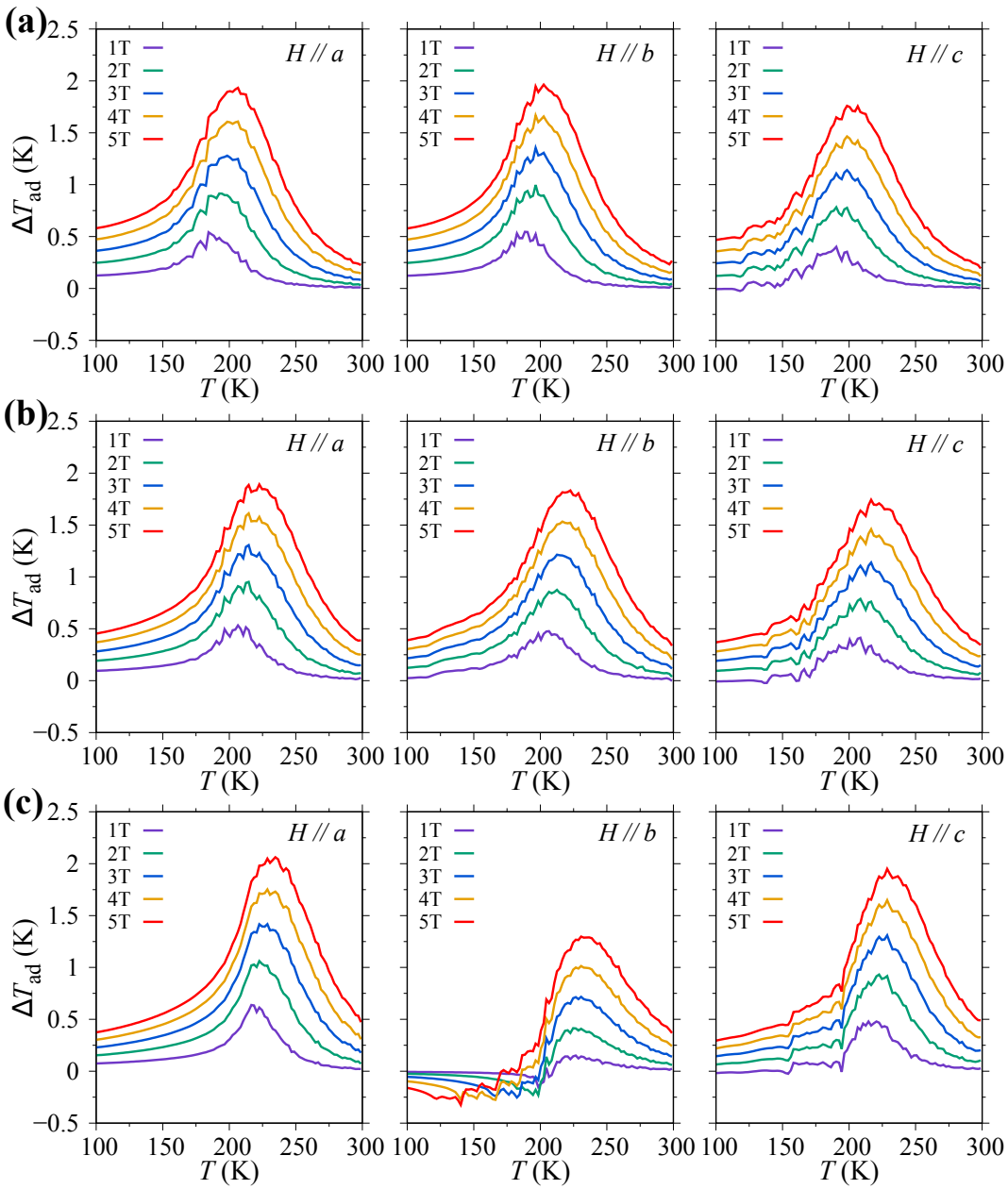


Fig. S15. Temperature dependences of ΔT_{ad} of monolayer (a) CrSCl, (b) CrSBr and (c) CrSI for $H \parallel a$, $H \parallel b$, and $H \parallel c$ in different magnetic fields, respectively.

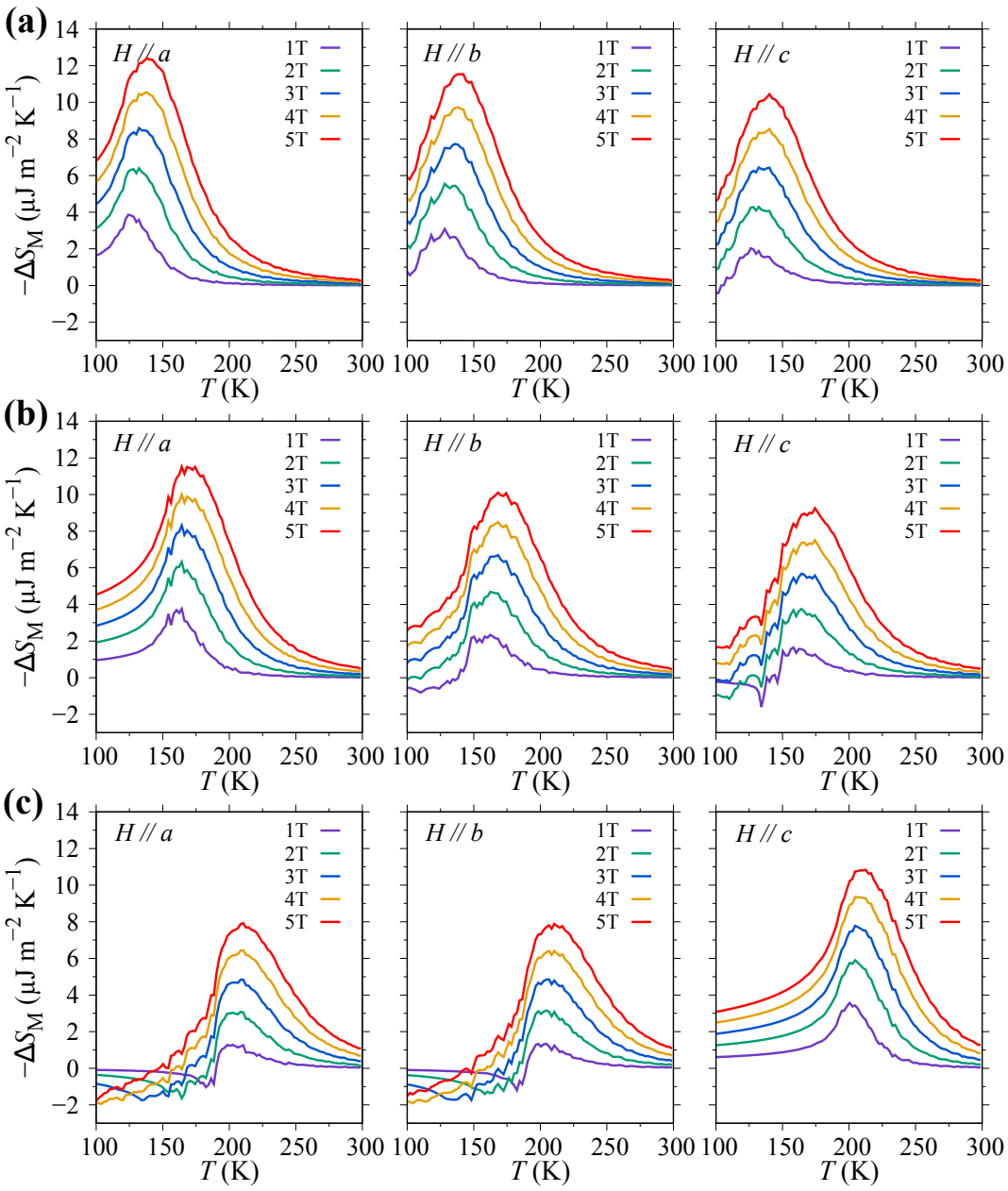


Fig. S16. Temperature dependences of $-\Delta S_{\mathrm{M}}$ of monolayer (a) CrSeCl, (b) CrSeBr and (c) CrSeI for $H \parallel a$, $H \parallel b$, and $H \parallel c$ in different magnetic fields, respectively.

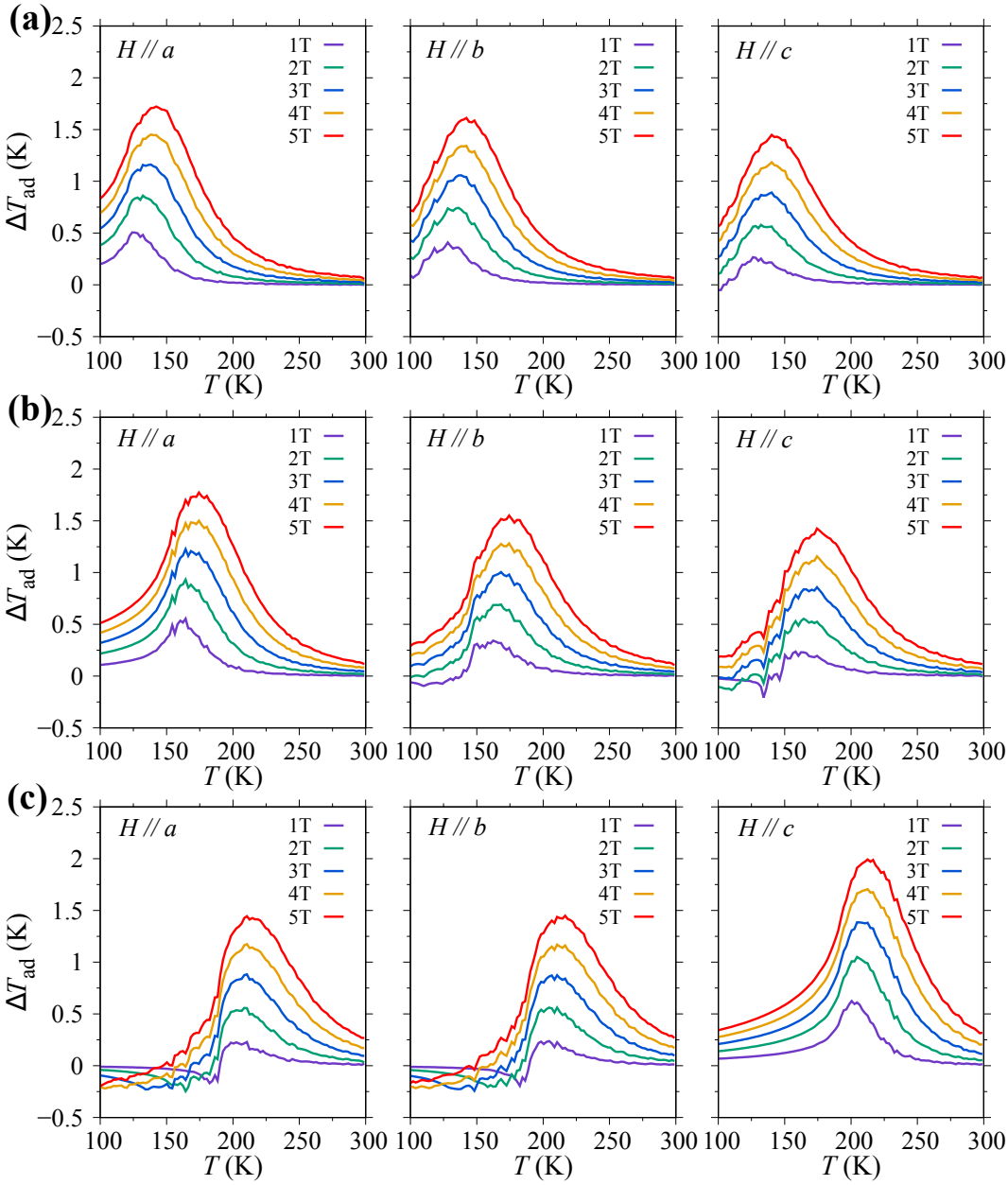


Fig. S17. Temperature dependences of ΔT_{ad} of monolayer (a) CrSeCl, (b) CrSeBr and (c) CrSeI for $H \parallel a$, $H \parallel b$, and $H \parallel c$ in different magnetic fields, respectively.

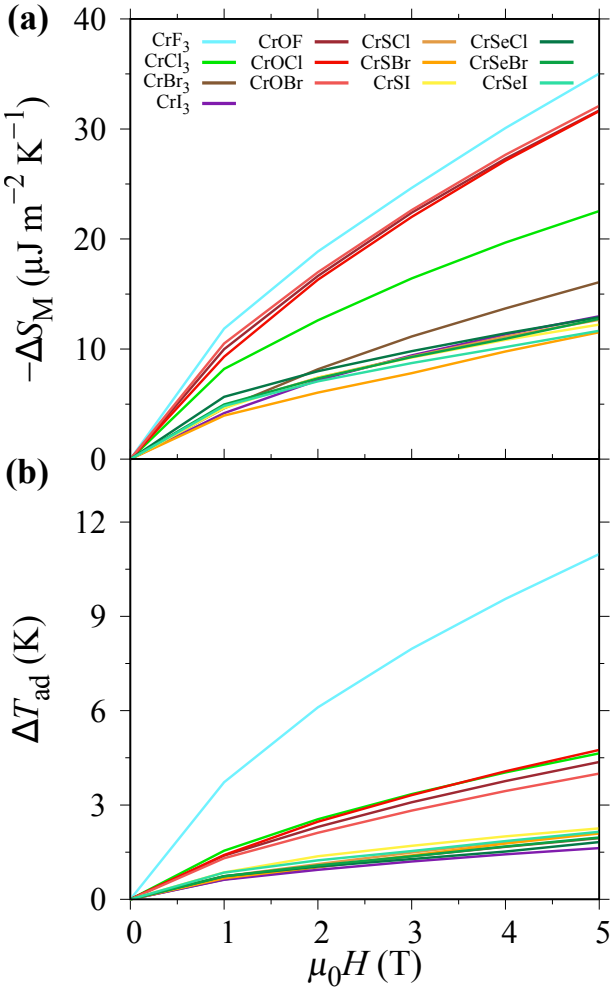


Fig. S18. Magnetic-field dependences of (a) $-\Delta S_{\mathrm{M}}^{\mathrm{max}}$ and (b) $\Delta T_{\mathrm{ad}}^{\mathrm{max}}$ of monolayers.

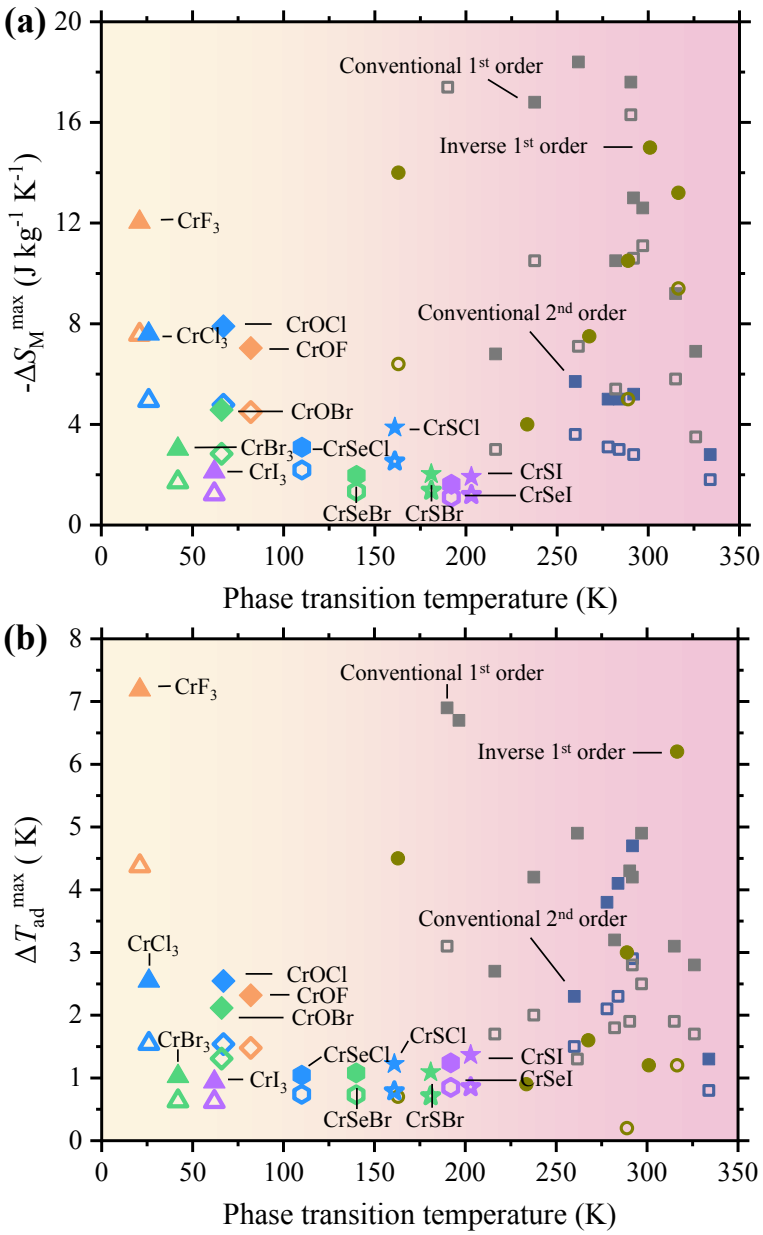


Fig. S19. The theoretical and ideal comparison of (a) $-\Delta S_{\mathrm{M}}^{\max}$ and (b) $\Delta T_{\mathrm{ad}}^{\max}$ between the monolayers and classical bulk magnetocaloric materials under low magnetic field (i.e., conventional 1st order materials, conventional 2nd order materials, inverse 1st order materials[5]). The hollow and solid points represent the data under 1 T and 2 T, respectively.

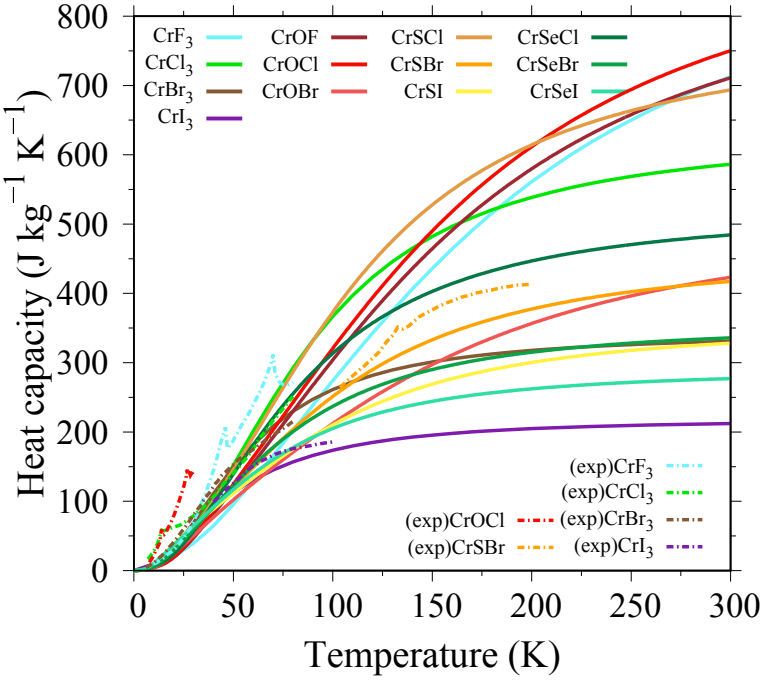


Fig. S20. Temperature dependences of heat capacity acquired by phonon calculations. The dashed lines are from previous bulk materials experimental measurements. The experimental data of single crystal of bulk CrF_3,[6] $CrCl_3$,[6] $CrBr_3$,[7] CrI_3,[3] CrOCl[8] and CrOBr[9] is drawn with dash lines.

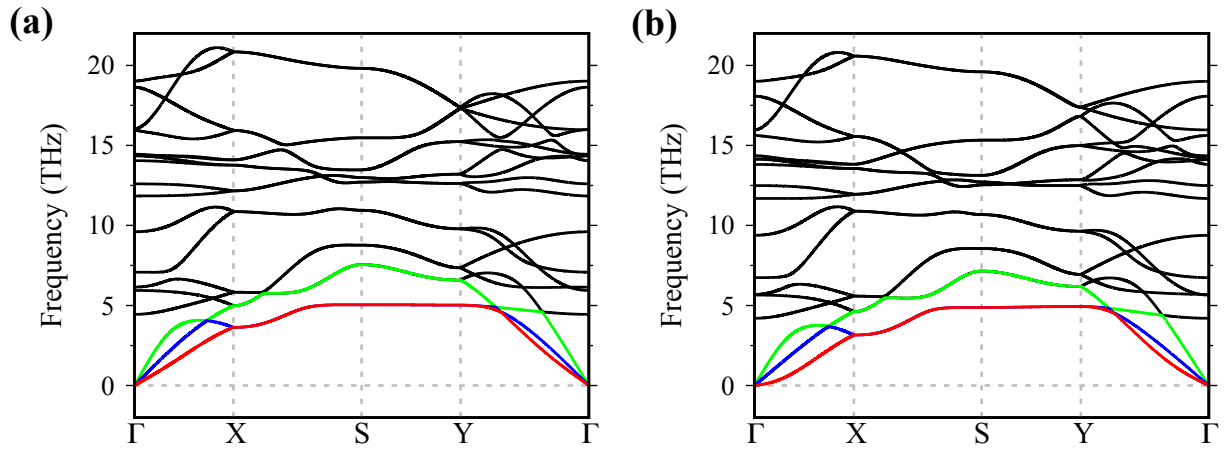


Fig. S21. Phonon dispersion spectra of monolayer CrOF under the 5% (a) *a*-axis and (b) *b*-axis compressive strain.

References

(1) Sadhukhan, B.; Bergman, A.; Kvashnin, Y. O.; Hellsvik, J.; Delin, A. Spin-lattice couplings in two-dimensional CrI_3 from first-principles computations. *Physical Review B* **2022**, *105*, 104418.

(2) Staros, D.; Hu, G.; Tiihonen, J.; Nanguneri, R.; Krogel, J.; Bennett, M. C.; Heinonen, O.; Ganesh, P.; Rubenstein, B. A combined first principles study of the structural, magnetic, and phonon properties of monolayer CrI_3. *The Journal of Chemical Physics* **2022**, *156*, 014707.

(3) Liu, Y.; Petrovic, C. Anisotropic magnetocaloric effect in single crystals of CrI_3. *Physical Review B* **2018**, *97*, 174418.

(4) Deng, Y.; Yu, Y.; Song, Y.; Zhang, J.; Wang, N. Z.; Sun, Z.; Yi, Y.; Wu, Y. Z.; Wu, S.; Zhu, J.; Wang, J.; Chen, X. H.; Zhang, Y. Gate-tunable room-temperature ferromagnetism in two-dimensional Fe_3GeTe_2. *Nature* **2018**, *563*, 94–99.

(5) Gottschall, T.; Skokov, K. P.; Fries, M.; Taubel, A.; Radulov, I.; Scheibel, F.; Benke, D.; Riegg, S.; Gutfleisch, O. Making a cool choice: The materials library of magnetic refrigeration. *Advanced Energy Materials* **2019**, *9*, 1970130.

(6) Hansen, W. N.; Griffel, M. Heat capacities of CrF_3 and $CrCl_3$ from 15 to 300 K. *The Journal of Chemical Physics* **1958**, *28*, 902–907.

(7) Yu, X.; Zhang, X.; Shi, Q.; Tian, S.; Lei, H.; Xu, K.; Hosono, H. Large magnetocaloric effect in van der Waals crystal $CrBr_3$. *Frontiers of Physics* **2019**, *14*, 6–10.

(8) Zhang, T. et al. Magnetism and optical anisotropy in van der Waals antiferromagnetic insulator CrOCl. *ACS Nano* **2019**, *13*, 11353–11362.

(9) Lee, K.; Dismukes, A. H.; Telford, E. J.; Wiscons, R. A.; Wang, J.; Xu, X.; Nuckolls, C.;

Dean, C. R.; Roy, X.; Zhu, X. Magnetic order and symmetry in the 2D semiconductor CrSBr. *Nano Letters* **2021**, *21*, 3511–3517.